

1 **Water ice in the dark dune spots of Richardson crater on Mars**

2

3 Kereszturi A.<sup>1</sup>, Vincendon M.<sup>2</sup>, Schmidt F.<sup>3</sup>

4

5 <sup>1</sup> Collegium Budapest, Institute for Advanced Study, H-1014 Budapest, Szentháromság 2.

6 Hungary

7 <sup>2</sup> Department of Geological Sciences, Brown University, Providence, Rhode Island, USA

8 <sup>3</sup> IDES, Université Paris-Sud 11; CNRS/INSU, Bâtiment 509, Université Paris-Sud, 91405

9 Orsay, France

10

11 **Abstract**

12

13 Interfacial liquid water has been hypothesized to form during the seasonal evolution of the  
14 dark dune spots observed in the high latitudes of Mars. In this study we assess the presence,  
15 nature and properties of ices – in particular water ice – that occur within these spots using  
16 HIRISE and CRISM observations, as well as the LMD Global Climate Model. Our studies  
17 focus on Richardson crater (72°S, 179°E) and cover southern spring and summer ( $L_S$  175° -  
18 341°). Three units have been identified of these spots: dark core, gray ring and bright halo.  
19 Each unit show characteristic changes as the season progress. In winter, the whole area is  
20 covered by CO<sub>2</sub> ice with H<sub>2</sub>O ice contamination. Dark spots form during late winter and early  
21 spring. During spring, the dark spots are located in a 10 cm thick depression compared to the  
22 surrounding bright ice-rich layer. They are spectrally characterized by weak CO<sub>2</sub> ice  
23 signatures that probably result from spatial mixing of CO<sub>2</sub> ice rich and ice free regions within  
24 pixels, and from mixing of surface signatures due to aerosols scattering. The bright halo  
25 shaped by winds shows stronger CO<sub>2</sub> absorptions than the average ice covered terrain, which

26 is consistent with a formation process involving CO<sub>2</sub> re-condensation. According to spectral,  
27 morphological and modeling considerations, the gray ring is composed of a thin layer of a few  
28 tens of μm of water ice. Two sources/processes could participate to the enrichment of water  
29 ice in the gray ring unit: (i) water ice condensation at the surface in early fall (prior to the  
30 condensation of a CO<sub>2</sub> rich winter layer) or during winter time (due to cold trapping of the  
31 CO<sub>2</sub> layer); (ii) ejection of dust grains surrounded by water ice by the geyser activity  
32 responsible for the dark spot. In any case, water ice remains longer in the gray ring unit after  
33 the complete sublimation of the CO<sub>2</sub>. Finally, we also looked for liquid water in the near-IR  
34 CRISM spectra using linear unmixing modeling but found no conclusive evidence for it.

35

36 Keywords: Mars, polar, ices, dunes, water

37

38 Corresponding author's email: akos@colbud.hu , tel.: 36-06-30-3437-876. fax: 36-1- 240-  
39 7708. Regular postal address: Collegium Budapest Institute for Advanced Study, H-1011  
40 Budapest, Szentharomsag u. 2. Hungary

41

42

## 43 **1. Introduction**

44

45 The aim of this work is to study the presence, origins and properties of water ice in the dark  
46 spots observed at the surface of the polar regions of Mars during local spring. These spots can  
47 give rise to flow-like features (Horvath et al. 2001, 2009). Assessing the presence and  
48 properties of water ice there is an important step while studying the possible contribution of  
49 liquid water to the formation of these features. The polar regions of Mars undergo a strong  
50 and rapid warming during spring (Kieffer and Titus, 2001). Local dark, sunlight absorbing  
51 environments such as the dark spots could be favorable environments for the formation of  
52 ephemeral liquid water on Mars if water ice is present at those locations during spring. It is  
53 already known that water ice is present at the kilometer scale in the seasonal and perennial ice  
54 caps of both hemispheres (Kieffer et al., 1976; Titus et al. 2003, Bibring et al., 2004). In the  
55 northern hemisphere, a water-ice ring follows the receding edge of the shrinking CO<sub>2</sub> ice cap  
56 (Kieffer and Titus, 2001; Bibring et al., 2005; Schmitt et al., 2005; Schmitt et al., 2006),  
57 partly because it appears from below the sublimated carbon dioxide seasonal cap and partly  
58 because it recondenses onto the perimeter of the remaining cold carbon dioxide ice (Wagstaff  
59 et al., 2008). On the contrary, no similar water ice annulus was observed in the southern  
60 hemisphere: water ice there consist of smaller water ice patches (Titus 2003, Bibring 2004,  
61 Titus, 2005; Langevin et al., 2006; Titus, 2008) which appear at the perimeter of the receding  
62 carbon dioxide cap, some of which remaining tens of kilometers away from the bright  
63 permanent CO<sub>2</sub> cap in summertime (Bibring et al., 2004). The high resolution imaging and  
64 spectroscopic dataset released by recent missions to Mars widen our ability to detect and  
65 study water in small, meter scaled environments such as the dark spots.

66

67 .

68

69 These Dark Dune Spots, which we abbreviate as DDS (Horváth et al., 2001; Gánti et al.,  
70 2003; Pócs et al., 2003), are part of the great number of strange seasonal features that appear  
71 during local spring in the polar regions of Mars, such as spiders (Kieffer, 2000; Kieffer et al.,  
72 2000; Ness and Orme, 2002; Piqueux et al., 2003; Christensen et al., 2005), dark spots (Malin  
73 et al., 1998, Malin and Edgett, 2001; Bridges et al., 2001; Zuber, 2003), flow-like features  
74 (Kieffer, 2003), Dalmatian spots (Kossacki and Kopystynski, 2004). Many of them could be  
75 the result of CO<sub>2</sub> gas outburst, but possibly other processes may also contribute like mass  
76 wasting (Hansen et al. 2010) or even flow of some liquid material (Möhlmann, Kereszturi  
77 2010). These phenomena potentially affect the CO<sub>2</sub> sublimation and may influence the  
78 climate at regional scale (Schmidt et al., 2009, Schmidt et al., 2010). We will present new  
79 observational evidence related to one of those phenomena, the Dark Dune Spots, to further  
80 test and constrain the different proposed scenarios of formation for those features.

81

82 Recent observations and theoretical computations have suggested that ephemeral liquid water  
83 or brines could be present on Mars. Based on theoretical calculations, above around 180 K  
84 thin interfacial water layer (Möhlmann 2004) and possible solid-state greenhouse warming  
85 may produce bulk brines (Möhlmann 2010). At the polar landing site of Phoenix, not only  
86 solid ice was observed, but also spherical droplet-like features, slowly changing with time on  
87 the leg of the lander, that may be composed of dense salty solutions (Renno et al. 2009a, b).  
88 Ephemeral flow-like features emanate from Dark Dune Spots (DDSs) that could be formed by  
89 flowing brines or thin water layer lubricated grains have been recently studied in the northern  
90 and southern polar regions (Kereszturi et al. 2010a, Reiss et al. 2010) – although other  
91 interpretations, like dry mass wasting and avalanches could also be possible (Hansen et al.

92 2010). These flow-like features based on their appearance, dark color, and elevated  
93 temperatures are good candidates for the formation of liquid water.

94

95 Here we analyze dark spot-like features on the wintertime formed frost layer, which are called  
96 DDSs and which can give rise to flow-like features (Horvath et al. 2001, 2009), located on the  
97 Richardson crater (72°S, 179°E). We study these features using CRISM (Compact  
98 Reconnaissance Imaging Spectrometer for Mars) and HiRISE data to argue whether water –  
99 ice or liquid – is present in some part of these spots. CO<sub>2</sub> ice, that form in the polar regions  
100 and may cold trap H<sub>2</sub>O molecules and enhances their concentration, will also be studied in  
101 details. The high imaging performances of HiRISE (High Resolution Imaging Science  
102 Experiment, maximal spatial resolution 30 cm) are combined with the water detection  
103 capabilities of the near-IR CRISM experiment. Observational constraints about the nature and  
104 distribution of ice are compared to climate modeling predictions. A scenario is then proposed  
105 to explain the origin and evolution of water ice in this region.

106

## 107 **2. Methods**

108

109 This section contains the background information about the data acquired by the CRISM and  
110 HiRISE cameras onboard Mars Reconnaissance Orbiter, as well as a description of the  
111 modeling methods used to interpret them.

112

### 113 **2.1 Observations**

114

115 We analyzed CRISM spectral data (Murchie et al. 2007), with CAT-ENVI software (Morgan  
116 et al. 2009) in Richardson crater (72°S 179°E) using CRISM “FRT” observations,

117 characterized by a high spatial and spectral resolution (18 m and 7 nm respectively). Near-IR  
118 wavelengths that range between 1 and 4  $\mu\text{m}$  were considered, and observations were corrected  
119 for photometry and atmospheric gas absorptions (McGiure et al. 2009). A filtering method  
120 (Parente 2008) is used to reduce noise. The interpretation of spectra measured by push-broom  
121 sensors may be influenced by the effect called “spectral smile”: the mean wavelength of  
122 spectels and the spectral resolution can slightly change from one spatial pixel to the next  
123 (Ceamanos, Douté 2009). We do not correct for the spectral smile because we take spectra  
124 near the center of the CRISM image where band shifts are lower than 0.002  $\mu\text{m}$  (Murchie et  
125 al. 2007), which has a minor impact on large absorption bands. The list of CRISM  
126 observations analyzed in this study is indicated in Table 1.

127

128 The CRISM spectral data were complemented by the analysis of the higher spatial resolution  
129 HiRISE images. We selected the highest resolution images acquired under proper illumination  
130 conditions to study the thickness of surface features using shadows (see Table 2.). We  
131 estimated absolute albedo values from HiRISE images, using the DN values of certain pixels  
132 from the RED channel images. We calculated the reflectivity with the formula  
133  $I/F=(DN*SCALING\_FACTOR)+OFFSET$ , and divided it with  $\cos i$ , which gives an  
134 approach of lambertian albedo.

135

136 The study of the spatial and temporal distribution of  $\text{H}_2\text{O}$  and  $\text{CO}_2$  ice is performed using  
137 band depth values, representing the absorption efficiency at certain wavelength region,  
138 characteristic for certain molecules and minerals. The following parameters were used to  
139 analyze ices: “BD1500” (1.5 micron  $\text{H}_2\text{O}$  ice band depth), “BD 1435” (1.435 micron  $\text{CO}_2$  ice  
140 band depth), and “ICER1” ( $\text{CO}_2$  and  $\text{H}_2\text{O}$  ice band depth ratio) defined by Pelkey et al. 2007  
141 (for detailed description of the calculation formulae see for the reference) on the basis of the  
142 parameters developed by Langevin et al. 2007. Very thin, micrometer thick layers of  $\text{H}_2\text{O}$  ice

143 can be detected in near-IR spectra (Schmitt et al., 1998), for instance using the characteristic  
144 absorption feature at 1.5  $\mu\text{m}$  (Bibring et al. 2004). The depth of this feature is measured by the  
145 “BD1500” spectral criteria.

146

## 147 **2.2 Spectral unmixing modeling**

148

149 The shape of the 1.5  $\mu\text{m}$  band of H<sub>2</sub>O ice is significantly controlled by temperature (Grundy  
150 and Schmitt, 1998) and grain size (Douté and Schmitt, 1998). Also, liquid water is spectrally  
151 distinct from water ice, with an absorption band at 1.5  $\mu\text{m}$  shifted by 0.05  $\mu\text{m}$  toward shorter  
152 wavelengths (Fig. 11). Other ubiquitous hydrated chemical species on Mars, such as sulfates,  
153 also have a band around 1.5  $\mu\text{m}$  (Langevin et al. 2005, Bibring et al., 2006, Fishbaugh et al.,  
154 2007, Massé et al. 2010). The possible presence of water ice with different grain size, liquid  
155 water and gypsum are therefore considered while conducting the spectral analysis.

156

157 We applied a strategy of sparse linear unmixing using the Fully Constraint Least Square  
158 (FCLS) suitable to unmix spectral mixture in the case of an overcomplete reference database  
159 (Heinz and Chang, 2001). Each observed spectra  $Y_k$  ( $k$  is the index of wavelength) is  
160 decomposed into a weighted sum of all reference spectra  $S_{jk}$  ( $j$  is the index of the reference  
161 spectra,  $j=1$  for CO<sub>2</sub>,  $j=2$  for H<sub>2</sub>O at 1 microns grain size, etc). The weight, or abundances,  $A_j$   
162 are assumed to be *summed to one* – because the sum of surface proportion is one - and *sparse*  
163 - with a distribution of zeros and only few non-zeros values.

164

$$165 \quad Y_k = \sum A_j S_{jk} \quad (1)$$

166

167

168 It means that if a spectrum is present in the database S but not present in the observed spectra  
169 Y, the method indicates a zero abundance. This property is especially suitable for our case  
170 because we do not expect all grain size of water ice, liquid water and gypsum (see later in the  
171 3.5 section) appearing at the same time. Due to the sum-to-one constraint, we add a flat bright  
172 and a flat dark spectrum that can model at first order aerosol contribution and dust  
173 contamination at the surface respectively. Abundances can be interpreted as surface  
174 proportion inside the pixel, if no non-linear mixing occurs. In a more likely case, intimate  
175 non-linear mixing should occur, leading to a significant shift between absolute abundances  
176 and actually estimated abundances with FCLS. Nevertheless, we will interpret the abundances  
177 A as “spectral abundances”. Such methodology is valuable to interpret global tendencies and  
178 for detection, but not for precise quantification.

179

## 180 **2.3 Climate modeling**

181

182 Observations of water and CO<sub>2</sub> ice at Richardson crater are compared with the predictions of  
183 the Global Circulation Model developed at the *Laboratoire de Météorologie Dynamique de*  
184 *Jussieu*. This model is able to predict the water cycle of Mars and has been validated against  
185 available datasets (Forget et al., 1999; Montmessin et al., 2004; Forget et al. 2008). The  
186 model computes the seasonal meteorology, notably the variations in water vapor and water ice  
187 precipitations, with a spatial sampling of 5x5° and a time step of half an hour. It is combined  
188 with a local energy balance code to predict the formation of ices on a given localized site with  
189 specific properties (Vincendon et al. 2010a, b).

190

## 191 **3. Results**

192

193 We first classify the observed features in section 3.1 using HiRISE images. Then, we analyze  
194 the spatial and temporal change in the properties of ice on the basis of their spectral properties  
195 as revealed by CRISM band ratio in section 3.2. In the section 3.3 we discuss how we assess  
196 the surface versus atmospheric origin of H<sub>2</sub>O spectral signatures. HiRISE and CRISM data  
197 are correlated in section 3.4. The results of the unmixing algorithm are discussed in section  
198 3.5. Modeling prediction of ice condensation based on climatologic and thermophysical  
199 considerations can be found in section 3.6. Finally, we discuss the possible scenarios for the  
200 origin of the observed features in section 3.7.

201

### 202 **3.1. Classification of observed albedo features**

203

204 There is a great number of various seasonal low albedo features on Mars in the polar region,  
205 including different dark spots (Malin et al., 1998; Malin and Edgett, 2000; Zuber, 2003,  
206 Kieffer et al., 2006; Kossacki et al., 2006), spider-like structures (Kieffer, 2000; Ness and  
207 Orme, 2002; Piqueux et al., 2003; Christensen et al., 2005) Dalmatian spots (Kossacki and  
208 Kopystynski, 2004), and Dark Dune Spots (DDSs) (Horvath et al., 2001; Ganti et al., 2003;  
209 Pocs et al., 2003). Here we analyze only one group, called Dark Dune Spots, and among them  
210 only the larger ones, which different sub-units could be resolved on CRISM images. There are  
211 various subsections of these spots, analyzed recently (Kereszturi et al. 2009, 2010) based on  
212 HiRISE images. Here we use the following classification:

213

- 214 • Dark features on the seasonal frost cover, with two groups (Fig. 1): 1. large spots  
215 (larger than about 20-40 m) are present only between the ridges of the dunes on  
216 horizontal surfaces, and 2. smaller spots, which are present on the dune ridges and

217 between them also, and on the slopes where flow-like features emanate from them  
218 (Horváth et al. 2009, Kereszturi et al. 2010).

- 219 • Here we analyzed only the large spots, large enough (i.e. > 60 m) to identify the  
220 following different sub-units of them from CRISM data:
  - 221 ○ *Dark core*: a roughly isometric and darkest area in the center, with albedo  
222 between 0.15-0.26 when the feature was evident before L<sub>S</sub> 250°. After this date  
223 the features diminished and the terrain becomes homogeneous.
  - 224 ○ *Gray ring*: a wide ring-like feature that surrounds the core, its albedo is  
225 intermediate between the dark core and the undisturbed frost cover, with  
226 albedo values between 0.25-0.30.
  - 227 ○ *Bright halo* (white collar): a region surrounding the spots brighter than the  
228 undisturbed average ice with albedo values between 0.37-0.24, somewhere  
229 elongated in downwind direction, possibly formed by refreezing process.
  - 230 ○ The *undisturbed ice* terrain surrounding far away the spots was also analyzed  
231 for control measurement.

232

233 These features show characteristic changes: first the dark core appears with dark wind-blown  
234 features emanating from it; later gray rings develop, then bright halos appear and finally the  
235 whole terrain defrosts (Fig. 2).

236

### 237 **3.2. Distribution and properties of ices from spectral analysis**

238

239 Three typical spectral CRISM observations of the 4 units (dark core, gray ring, bright halo,  
240 undisturbed ice) acquired during early to mid spring are analyzed in Figure 3. At that time  
241 near-IR H<sub>2</sub>O ice signatures are observed at every location, even in the darkest cores, while

242 based on the optical images no substantial surface ice is present. Very small quantity of water  
243 ice (a few  $\mu\text{m}$  thick) could produce observable signatures in the spectra without visible effect  
244 in optical images, and thin water ice clouds may also contribute to the observed signature.  
245 Moreover, dust contamination within the ice (e.g., if ice as condensed on a dust nuclei) can  
246 significantly reduce the albedo of ice, making it barely detectable in the optical while clearly  
247 seen in the near-IR (Kieffer, 1990; Vincendon et al., 2007).  $\text{CO}_2$  ice, detected on the basis of  
248 the 1.43  $\mu\text{m}$  band depth, is also present everywhere at that time. It has been shown by  
249 Langevin et al. 2008 that aerosols scattering is responsible for a mixing of surface spectral  
250 properties when remotely observed, which could contribute to some of the signatures  
251 observed in this region characterized by high spatial variations of surface properties at the 10s  
252 to 100s meters scale. This effect, often neglected, can however have a major impact on  
253 observations as surfaces surrounding a km size observed target could contribute to several 10s  
254 of % of the observed signal (Langevin et al. 2008).

255

256 The spatial distribution of  $\text{H}_2\text{O}$  and  $\text{CO}_2$  ices is outlined in Figure 4. This figure contains  
257 small insets of HiRISE PSP\_00307\_1080 (1 column) and CRISM image  
258 FRT000052BC\_07\_IF163L (2-4 columns). Different rows are for different locations inside  
259 Richardson crater. The distribution of the water ice band depth (BD1500) in the second  
260 column shows that water ice is located in the grey outer ring area of spots. The  $\text{CO}_2$  ice  
261 distribution is represented in the fourth column, showing that the darks spots are nearly  $\text{CO}_2$   
262 ice free, while the third column shows the areal distribution of the  $\text{H}_2\text{O}/\text{CO}_2$  ice ration  
263 (inverted ICER1 channel) which highlights that. the outer gray ring is water ice rich. The ice  
264 ratio is a bit lower in the dark central core than in the ring, but here based on the optical  
265 images very small amount of ice could be present and the atmospheric dust scatter may have a  
266 strong impact in the spectra. While assessing changes in the composition of the ice mixtures

267 from spectral analysis required the use of surface radiative transfer model (see e.g. Douté and  
268 Schmitt 1998; Skhuratov et al 1999; Hapke 2008 and reference herein), observing change in  
269 the ice band depth provides a first order idea of change occurring on the ground, keeping in  
270 mind that such changes can be due to several factors including grain size, photometry, and  
271 mixture type. CO<sub>2</sub> ice is nearly always present together with H<sub>2</sub>O ice, suggesting they could  
272 be mixed. But their ratio is changing, and could be correlated to the change in the appearance  
273 on visible images. CO<sub>2</sub> ice signatures are deeper in the bright halo and the undisturbed  
274 average icy surface, than in the darkest cores and the gray rings. The bright outer halo has the  
275 deepest CO<sub>2</sub> signatures compared to the average surface. The gray ring unit is relatively H<sub>2</sub>O  
276 rich and CO<sub>2</sub> poor, comparing their ratio to other unit types.

277

278 We highlight in Figure 5 the typical band depth change observed with time:

279

280 Changes of H<sub>2</sub>O ice based on BD1500 values:

- 281 • The different surface units show the same trend during L<sub>S</sub> 170° and 225°, except for  
282 the gray ring area.
- 283 • In the gray ring area the band depth increases from L<sub>S</sub> 180° until 220°, which is not  
284 observed for the other surface types, where nearly constant values are present.
- 285 • The water ice band depth is significantly lower for the dark core and bright halo in  
286 comparison to undisturbed terrain.
- 287 • After L<sub>S</sub> 225° there is a general decrease of the water ice band depth in all units which  
288 become spectrally similar.
- 289 • Water ice is confidently detected above the noise limit (~ 2%) until about L<sub>S</sub> 250°.

290

291 Changes of CO<sub>2</sub> ice based on BD1500 values:

- 292       • The depth of BD1430 increases from  $L_S$  170° until 225°, and then decreases.
- 293       • The bright halo feature shows stronger CO<sub>2</sub> ice signal than the other features,  
294       suggesting some re-condensation happened there after  $L_S$  210° (Titus et al., 2007).
- 295       • The CO<sub>2</sub> ice band depth is significantly lower for the dark core in comparison to  
296       undisturbed terrain.
- 297       • The CO<sub>2</sub> ice band depth is lower than the noise after about  $L_S$  250°.

298

299   Between  $L_S$  210° and  $L_S$  230°, the water ice band depth is higher relative to earlier and later  
300   periods in the gray ring unit. We discuss in the next section why this increase can be  
301   confidently attributed to surface bound ice.

302

### 303   **3.3. Separation atmospheric and surface H<sub>2</sub>O ice signatures**

304

305   An important but difficult issue is to separate water ice spectral signature of the surface from  
306   those of ice crystals in the atmosphere. There are attempts to separate the two sources by  
307   spectral calculation using the size dependent spectral properties of water ice in the 3  $\mu$ m range  
308   (Langevin et al., 2007; Carrozo et al., 2009). However, no methods provide firm separation  
309   yet.

310

311   Another approach relies on the analysis of the spatial distribution of H<sub>2</sub>O ice signatures.  
312   Localized increase of the ice signatures associated with specific tens of meters scale  
313   morphological features is indicative of a surface origin of the ice signature. While conducting  
314   this kind of analysis, one should however carefully consider the role of potential photometric  
315   effect: the apparent spectral signature of a widespread ice cloud can also change as a function  
316   of the surface type over which it is observed. For example, ice cloud signatures can be

317 enhanced when observed above a tilted surface in shadow, as such a surface will be mainly  
318 illuminated by light scattered by the atmosphere, which contain the ice cloud signature. In  
319 Figure 6, we show that the spectral signatures of H<sub>2</sub>O ice observed in the gray ring area can  
320 be confidently attributed to the surface, as it localized, repetitively observed for each spot, not  
321 associated with lighting conditions, and as no suspicious trends with albedo are observed  
322 (both the darker and brighter areas around the grey ring show lower water signatures).

323

#### 324 **3.4. CRISM - HiRISE correlation**

325

326 We analyzed in detail the HIRISE image PSP\_003175\_1080 which is characterized by a high  
327 spatial resolution, a low noise, and a low solar elevation above the horizon (to make long  
328 shadows). It has been obtained at L<sub>S</sub> 210° (mid spring). Although it is not easy to interpret the  
329 illumination based topography of the terrain with changing frost cover in springtime, we think  
330 a small topographic step along the perimeter of the gray ring is detectable in the image: the  
331 surrounding brighter ice is elevated, while the area of the gray ring (as well as the darkest  
332 core) is at lower topographic level. We are now going to detail the analysis of dark shadowed  
333 and bright illuminated sections of the terrain that lead to this result.

334

335 To find out the topography from illumination, both the intrinsic albedo of the surface material  
336 and the exposure of the surface slope toward the direction of solar insolation should be taken  
337 into account, as both may contribute to the observed brightness of any point of the images.

338 We identified five surface unit types based on relative brightness differences, labeled from 1  
339 (the brightest) to 5 (the darkest) (see Figure 7). This analysis was realized on the above  
340 mentioned PSP\_003175\_1080 image with good spatial resolution. The following brightness  
341 categories were identified:

- 342 1. the brightest unit (DN values 600-530). This unit type covers only small part of the  
343 images and is located always right next to unit 2 (see below). It is located along the  
344 perimeter region of the spots. Members of this group are usually elongated roughly  
345 from the lower left to the upper right, in right angle to the direction of the solar  
346 illumination.
- 347 2. average brightness unit (DN values 580-460). This unit makes up most of the terrain  
348 surrounding the dark spots and probably consists of CO<sub>2</sub> ice.
- 349 3. moderately bright unit (DN values 440-300). It covers the outer gray ring of the DDS,  
350 4. darker unit (DN values 460-240). Often elongated from the lower left to the upper  
351 right, also in right angle to the solar illumination. Besides the elongated ones this unit  
352 is also present on the left or top-left side of small, isolated and nearly isometric  
353 patches of unit 2.
- 354 5. darkest unit (DN values 130-40). It is present at the center of DDSs, where probably  
355 the barren, defrosted dark basaltic dune surface is visible.

356

357 We have derived the following conclusions based on the relative location of these brightness  
358 units:

- 359 • unit 1 and unit 3 frequently run parallel to each other on the right and left side of unit 2  
360 respectively (Fig. 8. a1, a2, b1). Such appearance is expected if they are the solar  
361 facing (1) and shadowed (3) units respectively, produced by elevated and elongated  
362 CO<sub>2</sub> ice stripes,
- 363 • when units 1 and 2 form isolated, nearly isometric patches, unit 3 is also present at the  
364 left or top-left side of these brighter CO<sub>2</sub> “icebergs”, also suggesting unit 3 is  
365 composed of shadows,

- 366       • unit 5 is only present in the center of DDSs, which represent a feature independent of  
367       the CO<sub>2</sub> ice cover, and probably show barren dark dune surface without any kind of  
368       ice.
- 369       • unit 4 covers only the outer ring of the DDSs where unit 1 or 2 are present, and is not  
370       present in the immediate surrounding of the unit 5. It also strengthens the possibility  
371       that it is the shadow of elevated CO<sub>2</sub> ice features.

372

373 To summarize, as unit 4 is always on the left or top-left side of unit 2, and it is also often  
374 elongated parallel to unit 1, unit 4 probably represents the shadow of thick CO<sub>2</sub> ice (Fig. 8. a1,  
375 a2, b2). In this case the shadows could be used for the rough determination of thickness of  
376 CO<sub>2</sub> ice. For such measurement it is important to note that at some locations the elongated  
377 heights are composed of both the solid dune ripples below the CO<sub>2</sub> ice cover and the ice cover  
378 itself together (like Fig. 8. a1, a2). In these cases the height measurement would show not  
379 only the thickness of CO<sub>2</sub> ice but also the height of the dune ripple. But there are many  
380 examples where small isolated heights (such as units 1 and 2) and their shadows (unit 3) are  
381 present together, and no ripple-like feature is visible in their surroundings (Fig. 8. d1, d2, f1,  
382 f2). In these cases the heights are probably only the results of the unit 2 composed of CO<sub>2</sub> ice,  
383 and here the height estimation shows the thickness only of the CO<sub>2</sub> ice. It is also visible that  
384 bright units and darker shadows are present together close to the circular edge of dark spots,  
385 as one would expect if the CO<sub>2</sub> ice cover of the surrounding terrain begins here.

386

387 It is also possible that at some locations the surface albedo changes producing the difference  
388 in brightness, e.g. in the case of Fig. 8a1 where depressions on the left between dune ripples  
389 could be darker because of accumulated dark dust. But as the solar facing side of the bright  
390 unit is also present there, real topographic undulation should be present with solar facing

391 bright slopes, and also with opposite facing shadowed slopes. And there are such cases (like  
392 Fig. 8. b2, c1, d1, d2, f1, f2) where it is very improbable that dust accumulated only on the  
393 shadowed sides of isolated bright patches. More probable explanation is that these dark  
394 features are shadows.

395

396 The shadow-like unit 3 always surrounds small isometric or larger elongated heights and  
397 always elongated toward the left or top-left. During the acquisition of the image the Sun was  
398  $24^\circ$  above the horizon toward the lower right. The shadows' average length is about 20-30  
399 cm, so the bright ice layer covering the whole terrain except the spots is roughly about 10 cm  
400 high.

401

402 To exclude the effect that earlier formed and permanent depressions are visible in the images  
403 (and not annually reoccurring features) we compared images acquired before the spot  
404 development with later images contain dark spots. On the earlier images PSP\_002186\_1080  
405 and PSP\_003175\_1080 of the same area, acquired during continuous CO<sub>2</sub> frost coverage (at  
406  $L_S$   $166.20^\circ$  and  $210.6^\circ$  respectively) no spot or any topographic depression is visible. The lack  
407 of such depression suggests that the gray rings' area was covered originally with the layer that  
408 was at least 10 cm thick at that time, which disappeared later and formed the depression; the  
409 original thickness could have been even larger, as CO<sub>2</sub> ice may have already started to  
410 sublimate at the time of the shadow measurement. Unfortunately the earlier image's  
411 resolution is substantially lower than the analyzed one, and all later images showing  
412 summertime defrosted surface were acquired under bad illuminating conditions, and they can  
413 not be used to analyze the topography in details. Figure 9. a) shows the earlier image of a  
414 terrain in Richardson-crater with complete CO<sub>2</sub> ice coverage, the b) shows the later image  
415 with several dark spots. The same boxed areas are magnified in c) and d) subsets. The

416 continuous ice cover is visible in c), while CO<sub>2</sub> ice free, but still H<sub>2</sub>O ice covered areas can be  
417 seen in the d) subset. Arrows show dune ripples, which are present on the CO<sub>2</sub> ice covered  
418 and in the CO<sub>2</sub> ice free terrain too. The shadows by the CO<sub>2</sub> ice cover are marked with arrow  
419 heads in subset d). It can be seen that even the topography of the ripples might affect the  
420 shadow length, the CO<sub>2</sub> ice layer definitely cast shadows. As it was shown earlier (see Figure  
421 8.), there are such small, isolated, nearly isometric CO<sub>2</sub> heights, where no dune ripples below  
422 them affected the height of the CO<sub>2</sub> ice, and the thickness estimation based on shadows. The  
423 gray ring area is not barren dark opposite to the central core, suggesting some ice cover is still  
424 there. The gray layer is substantially thinner than the brighter CO<sub>2</sub> ice.

425

426 The location of the deepest H<sub>2</sub>O ice signatures that could be confidently attributed to the  
427 surface (see section 3.3) based on CRISM data coincides with the gray ring features seen in  
428 the HIRISE data (Fig. 10). In this area the small-scale dune ripples are also visible. This  
429 observation is compatible with the idea that condensed H<sub>2</sub>O covers the surface there in a thin  
430 layer, which allows the topographic undulation of the surface to remain visible. The grey ring  
431 area also contains weaker CO<sub>2</sub> ice signatures. It has been shown by Langevin et al. 2008 that  
432 aerosols scattering are responsible for a mixing of surface spectral properties when remotely  
433 observed. In particular, an ice free area of limited extent (< km) surround by a widespread ice  
434 rich area will contain ice signatures when seen from orbit as a result of the mixing of spectral  
435 properties by aerosols scattering. Surrounding icy areas will typically represent 10 to 30% of  
436 the observed signal (Langevin et al. 2008). As a consequence, the grey ring area could be free  
437 of CO<sub>2</sub> ice as it is of small extent, characterized by the weakest CO<sub>2</sub> signatures of the area  
438 (see Figure 4 and Figure 6) and surrounded by terrains with strong CO<sub>2</sub> ice signatures.  
439 Moreover, in Figure 11 we show HiRISE images of the dark spots showing bright patch  
440 consistent with ice located within the dark spots. These cm-dm size patches are below the

441 CRISM resolution. As a consequence, spatial mixing could also contribute to the CO<sub>2</sub> ice  
442 spectral signature seen by CRISM in the dark spots and grey ring, which could be mainly CO<sub>2</sub>  
443 ice free in mid spring.

444

### 445 **3.5. Spectral unmixing results**

446

447 Using the FCLS linear unmixing method, we study the properties of this ice layer and we  
448 notably test the possible presence of liquid water in the four identified units. We consider 6  
449 endmembers spectra (water ice with 3 grain size, CO<sub>2</sub> ice, liquid water and gypsum) which  
450 are representative of the expected potential surface components and which have a significant  
451 impact on the 1.5 μm spectral regions (see Figure 12 and section 2.1). CO<sub>2</sub> and H<sub>2</sub>O ices have  
452 been modeled by a radiative transfer simulation (Douté and Schmitt, 1998) using optical  
453 constant recorded in the laboratory (Schmitt et al., 1998). Both gypsum and liquid water have  
454 been acquired at Labotaroire de Planétologie de Grenoble (Schmitt and Pommerol,  
455 unpublished). These spectra will be soon available online at <http://ghosst.obs.ujf-grenoble.fr>.  
456 Two spectrally blank spectra are also considered to account for dust and aerosols. Also an  
457 atmosphere transmission spectrum has been added to take into account, small residue of the  
458 atmosphere removal.

459

460 We estimate the abundance of each reference spectra (see Fig. 12) for the CRISM images:  
461 43A2 (L<sub>S</sub>=181.7°), 52BC (L<sub>S</sub>=213.7°), 56CO (L<sub>S</sub>=221.0°), 5C94 (L<sub>S</sub>=241.7°), 5E38  
462 (L<sub>S</sub>=245.5°), 5FF6 (L<sub>S</sub>=248.7°) and 6516 (L<sub>S</sub>=262.6°). We used the range 1.04-1.38 μm and  
463 1.51-2.13 μm to remove the narrow CO<sub>2</sub> feature that could be affected by the spectral smile.  
464 We also weight by a factor of 5 the spectral range 1.50-1.53 μm, very sensitive to water ice,

465 liquid water and gypsum. The root-mean-square (rms) is then computed without weight. All  
466 results for the model are shown in the Appendix A.

467

468 The general trend of the total H<sub>2</sub>O ice spectral abundance (sum of H<sub>2</sub>O with grain size of 1  
469 and 100 μm) is compatible with the band ratio (Fig. 5 top). Water ice at 1 cm grain size is  
470 never detected. The relative fraction of 1 μm grain size is plotted in Figure 13. The dark core  
471 has the smallest mean grain size of the four units. The higher grain sizes are identified in the  
472 undisturbed terrain. Figure 13 suggests a general trend with increasing grain size until L<sub>S</sub>=  
473 220° and then decreasing until L<sub>S</sub>=240°. These facts indicate that: (i) water ice is present with  
474 relative low grain size, consistent with seasonal ice; (ii) the grain size is evolving with time,  
475 which can be due to several mechanisms including resurfacing by sublimation,  
476 recondensation during the night, sublimation or deposition by geyser activity, grain  
477 metamorphism.

478

479 The results show that the spectral abundance of CO<sub>2</sub> ice is decreasing from 10% to 3% in  
480 agreement with band ratio BD1430 (Fig. 5 bottom). Also, the fit of CO<sub>2</sub> ice bands is  
481 compatible with large grain size (10 cm) and possibly a translucent slab ice. The last  
482 observation 6516 shows an estimated abundance of 0.06%, probably due to atmospheric  
483 residue.

484

485 We have also included liquid water and gypsum – a mineral with a 1.5 microns band  
486 resembling that of liquid water - in our modeling procedure. In Figure 14, we show one  
487 example of the model results for the dark spot of image 56CO for three linear unmixing  
488 scenarios: (1) without liquid nor gypsum (2) with liquid water only (3) with liquid water and  
489 gypsum. The rms is decreasing from model 1 to model 3 due to a slightly better fit of the 1.5

490 microns band (see Figure 14). This tends to indicate that a spectral component with a water  
491 band shifted toward shorter wavelengths, such as gypsum or liquid water, could be present.  
492 Sulfates and/or liquid water have been detected in six over the seven images considered (i.e.:  
493 for all observation except the last one at  $L_S=262.6^\circ$ ) in the “dark center” region, while it is  
494 almost never detected in the average terrain or in the bright halo. However, retrieved  
495 abundances are low ( $< 3\%$ , see Appendix A), and differences in modeled spectra are not  
496 significant given the first order method employed here (Figure 14). Although the retrieval of a  
497 few % of species with a 1.45 microns band consistent with liquid water in the dark spots only  
498 is intriguing, no robust conclusions can be reached. Moreover, none of the ratio spectra show  
499 evidence for liquid water or gypsum (see Fig. 15). To assess more precisely the possible  
500 presence of liquid water and/or gypsum in CRISM spectra, a non-linear spectral inversion  
501 using radiative transfer model should be performed in the future.

502

### 503 **3.6. Climate modeling results**

504

505 The surface stability and presence of ices are analyzed at the latitude of Richardson crater as  
506 the season progresses from winter to summer using a climatic model (see section 2 for  
507 details). Three modeling hypotheses concerning local surface properties are shown in Fig. 16:  
508 (A) diamonds for standard parameters (flat surface, moderately bright ices), (B) stars for  
509 condensation on a  $15^\circ$  pole facing slope (to estimate the effect of local favorable conditions),  
510 (C) triangles for "dark" ice (albedo of 0.25 for both  $H_2O$  and  $CO_2$  ice, a rough attempt to  
511 assess the impact of dust contamination of ice). These modeling predictions are compared to  
512 the presence or absence of ices at Richardson crater as a function of season as constrained  
513 from CRISM data, which show a general good agreement between data and model.

514

515 Water ice accumulation starts before CO<sub>2</sub> ice at the beginning of fall, mainly due to snow  
516 precipitation of small grain size particles (more than 99% of the total water ice accumulation)  
517 that have condensed in the lower atmosphere according to the simulation (see also Forget et  
518 al., 2006). A thin layer of a few microns to a few 10s of microns thick H<sub>2</sub>O ice below the CO<sub>2</sub>  
519 ice is expected according to model results, as noted by Schmitt et al. 2009. Then both ices  
520 condense simultaneously (H<sub>2</sub>O inclusion within the CO<sub>2</sub> ice) 20 to 30° of L<sub>S</sub> later. As a result  
521 we have a layered structure: only H<sub>2</sub>O ice below, and CO<sub>2</sub> plus H<sub>2</sub>O ice above. The ratio of  
522 H<sub>2</sub>O ice in the upper layer depends on several factors, above all meteorological conditions  
523 and global atmospheric circulation, as during the CO<sub>2</sub> condensation in southern winter the  
524 average atmospheric vapor content reaches maximum supplied by the exposed northern  
525 permanent water ice cap. When cold CO<sub>2</sub> ice is present, it traps available water vapor. Ice  
526 disappears prior to the summer solstice even for favorable conditions. According to the  
527 model, water ice remains 5° to 10° of L<sub>S</sub> later compared to CO<sub>2</sub>. The contamination of ice by  
528 dust significantly decreases the stability of ice in spring, which sublimation is shifted by about  
529 30° of L<sub>S</sub>. According to the model, CO<sub>2</sub> ice disappears at L<sub>S</sub> 220° for a moderately dark ice  
530 with a 0.25 albedo (Figure 16). This is consistent with the morphological and spectral  
531 analyses conducted above, showing that at a similar period (L<sub>S</sub> 210°, see section 3.4) the grey  
532 ring is composed of an H<sub>2</sub>O ice rich thin layer while surrounding areas are still covered by a  
533 thicker layer of CO<sub>2</sub> ice.

534

### 535 **3.7. Formation mechanisms of H<sub>2</sub>O in the gray outer area**

536

537 Based on the observations and modeling predictions presented in the previous sections, we  
538 propose the following scenario for the formation of the observed surface H<sub>2</sub>O ice in the dark  
539 dune spots of Richardson crater:

540  
541  
542  
543  
544  
545  
546  
547  
548  
549  
550  
551  
552  
553  
554  
555  
556  
557  
558  
559  
560  
561  
562  
563  
564

1. During early fall, H<sub>2</sub>O deposits start to form at the surface. They are mainly composed of precipitations that have settled from the lower atmosphere. Several tens of μm of water ice accumulate at the surface (see section 3.6).
2. During mid-fall, concomitant condensation of H<sub>2</sub>O and CO<sub>2</sub> begin and form a layer of CO<sub>2</sub> ice contaminated by H<sub>2</sub>O ice. Several tens of cm of frost, mainly composed of CO<sub>2</sub> ice, form in the whole area during that period according the earliest CRISM observations, the HiRISE observations of a 10 cm depression in mid-spring (section 3.2) and the modeling predictions (see section 3.6).
3. After the spring equinox, dark core are observed at Richardson crater. They probably result from the formation of CO<sub>2</sub> jets below the translucent ice (Kieffer, H.H., 2000), which carry along dune grains that settle about the jet. This scenario is in agreement with the results from the linear unmixing method: (i) detection of large CO<sub>2</sub> ice grain size; (ii) higher abundances of dark dust for the dark core and grey ring units (see section 3.5). Around the dark spot a “grey ring” is observed, which spectral composition during mid-spring is consistent with an enhanced amount of water ice (see section 3.3) and probably no CO<sub>2</sub> ice. Two possible scenarios can then explain or contribute to the observed properties of this grey ring:
  - a. The presence of dark dust material fallen from the jet increases surface absorption and is responsible for ice sublimation. Ice sublimates faster at the center of the spot, which explain the depression observed in HiRISE images and the weak CO<sub>2</sub> ice bands observed in CRISM data for which spatial mixing of ice-free and ice-rich subpixel deposits, as well as aerosols scattering, is a probable explanation (see section 3.4). In the outer grey area, albedo is higher and causes higher stability of water ice, as indicated by the model (see Fig.

565 15). The relative smaller water ice grain size could be due to the reappearance  
566 of the small grain size layer of snow precipitated in early fall.

567 b. The water ice, that is present between the sand substrate and the translucent  
568 CO<sub>2</sub> ice layer, is blown up with sand grains by geyser activity (Kieffer 2000,  
569 Piqueux et al. 2003). Water ice grain falls on the top of the surface surrounding  
570 the central dark core, contributing to the formation of the water ice rich grey  
571 ring. The relative smaller water ice grain size could be due to the geyser  
572 activity.

573 4. Although no robust evidence for liquid water has been found in the spectra, the data  
574 are not inconsistent with the possible presence of small amount of liquid water in the  
575 dark core unit and, with an even lower probability, in the grey ring unit (see section  
576 3.5).

577

#### 578 **4. Conclusions**

579

580 We have performed a study of the Dark Dune Spots observed in Richardson crater using  
581 HiRISE and CRISM data. Our goal was to identify and analyze the presence of water ice  
582 within these features. It has been possible to analyze the largest spots using the 20 m spatial  
583 resolution of CRISM, which provided clues about the presence of water ice within these  
584 features. In particular, Dark Dune Spots can give rise to flow-like feature and the role of  
585 liquid water in this process is the subject of ongoing research.

586

587 Based on the analysis of HiRISE images, we identified three characteristic sections of Dark  
588 Dune Spots observed in Richardson crater during spring: dark core, gray ring and bright halo.

589 We used time series of CRISM images between L<sub>S</sub> 175.5° and L<sub>S</sub> 340.5° to analyze temporal

590 changes of H<sub>2</sub>O and CO<sub>2</sub> related band depth values. At the area of gray rings on HiRISE  
591 images the bright icy layer that surrounds the spots is missing. Based on shadow length  
592 measurements an about 10 cm deep horizontal depression is present there, measured relative  
593 to the top of surrounding bright ice cover. These depressions were not present in earlier  
594 images, suggesting it forms due to the localized sublimation of the ice layer.

595

596 We identified H<sub>2</sub>O and CO<sub>2</sub> ice at most locations during spring, but with significant spatial  
597 and seasonal variations in band depth and linear unmixing results. Spatial subpixel mixing,  
598 water ice cloud contribution, and aerosols scattering responsible for an apparent mixing of  
599 surface properties must be carefully considered while analyzing the apparent spectral  
600 properties in CRISM data. Enhanced water ice signature is observed during mid-spring at the  
601 gray ring area from BD1500 values. Based on the size of these ring features (20-30 m) and on  
602 the repeatability of these features from one spot to the next, the surface origin of this water ice  
603 has been confidently determined.

604

605 By analyzing CRISM images, HiRISE data and the result of a climate model, it has been  
606 possible to build a scenario for the formation and evolution of the ice layers in and around the  
607 dark dune spots of Richardson crater. During fall thin, tens of  $\mu\text{m}$  thick H<sub>2</sub>O ice rich layer  
608 forms at the surface. 30° of L<sub>S</sub> later a layer of CO<sub>2</sub> ice with inclusions of H<sub>2</sub>O ice forms on top  
609 of it, and reach a thickness of a few tens of cm. During late winter / early spring the dark spots  
610 form, probably by geysers activity (Kieffer, 2000) in agreement with the large CO<sub>2</sub> grain size  
611 detected by the linear unmixing. A bright halo-like feature surrounds the spot and show  
612 stronger CO<sub>2</sub> signature than the undisturbed average ice-covered surface, suggesting CO<sub>2</sub> was  
613 refrozen there. The dark spots and the grey rings are located in a 10 cm thick depression  
614 compared to the surrounding bright, ice-rich layer. The dark center spot is ice-free at some

615 places (but contain ice signatures in CRISM images due to spatial mixing and aerosols  
616 scattering). At  $L_S=210-230^\circ$ , the gray ring area is covered by an enhanced thin layer of H<sub>2</sub>O  
617 ice. The origin of H<sub>2</sub>O may be from two sources: (i) condensation on the surface in autumn  
618 (before the formation of CO<sub>2</sub> layer) or during winter time (CO<sub>2</sub> layer acting as a clod trap)  
619 and exhumed by the differential sublimation of CO<sub>2</sub> and H<sub>2</sub>O ice (ii) H<sub>2</sub>O attached to the sand  
620 grains that are blown up by geyser activity and that fall at the surface around the spot.

621

622 We observed H<sub>2</sub>O ice left behind the disappearance and/or reduction of CO<sub>2</sub> ice thickness in  
623 the gray ring area of Dark Dune Spots. Resembling situation was observed as a shrinking H<sub>2</sub>O  
624 ring during the recession of the northern seasonal cap (Appéré et al., 2008, Wagstaff et al.  
625 2008), and in some patches at the southern hemisphere too (Brown et al. 2010), but at  
626 substantially larger spatial scale.

627

628 The presence of water ice in physical contact with insolated dark dune material could lead to  
629 the formation of liquid water. Such environments are of interest while assessing the potential  
630 for habitability of present day Mars (Szathmary et al. 2007). In the gray ring area the water ice  
631 surrounds darker surface, where liquid interfacial water layer or brine (Möhlmann 2004,  
632 2009, 2010) may form. We found no firm evidence for the presence of liquid water in near-IR  
633 spectra, although linear unmixing results show that the data are not inconsistent with a  
634 possible slight contribution (a few %) of liquid water in the dark core unit.

635

636 The above-mentioned observations may have important impact on the explanation of other  
637 circumpolar features, showing water ice may be present in CO<sub>2</sub> ice free regions at the  
638 southern hemisphere of Mars. We observed the presence of water ice in physical contact with  
639 relative dark dune grains in 100-200 meter sized spots. In their surrounding of these spots in

640 Richardson crater flow-like features are present emanate from resembling but smaller spots,  
641 which are too small to be resolved by CRISM. If resembling process happen there, such  
642 locations could be also interesting for the possible ephemeral presence of water ice, as well as  
643 other seasonal features should be analyzed in detail to search for water ice there.

644

## 645 **5. Acknowledgment**

646

647 The authors would like to than Bernard Schmitt and Francois Forget for their help. This work  
648 was supported by the ESA ECS-project no. 98076. This work was also supported by the  
649 Centre National d'Etudes Spatiales (CNES). It is based on observations with CRISM  
650 embarked on MRO. We also acknowledge partial support from the Programme National de  
651 Planétologie (CNRS/INSU).

652

## 653 **6. Abbreviations**

654

655 CRISM - Compact Reconnaissance Imaging Spectrometer for Mars, DDS - Dark Dune Spot,  
656 FCLS - Fully Constraint Least Square, HiRISE - High Resolution Imaging Science  
657 Experiment,  $L_S$  - solar longitude, rms - root-mean-square, LPG – Laboratoire de Planétologie  
658 de Grenoble, FCLS – Fully Constrained Least Square

659

## 660 **7. References**

661

662 Appéré, T., Schmitt, B., Pommerol, A., Douté, S., Beck, P., Forget, F., Schmidt, F., Langevin,  
663 Y., Bibring, J.-P., Gondet, B., 2008. Spatial and Temporal Distributions of the Water Ice

664 Annulus During Recession of the Northern Seasonal Condensates on Mars. Third  
665 International Workshop on The Mars Atmosphere, Abstract .9008.  
666  
667 Bibring, J.-P., Langevin, Y., Gendrin, A., Gondet, B., Poulet, F., Berthé, M., Soufflot, A.,  
668 Arvidson, R., Mangold, N., Mustard, J., Drossart, P., the OMEGA team, 2005. Mars Surface  
669 Diversity as Revealed by the OMEGA/Mars Express Observations, Science 307. 1576 –  
670 1581.  
671  
672 Bibring, J.-P., Langevin, Y., Poulet F., Gendrin A., Gondet B., Berthé M., Soufflot A.,  
673 Drossart P., Combes M., Bellucci G., Moroz V., Mangold N., Schmitt B. & the OMEGA team  
674 2004. Perennial water ice identified in the south polar cap of Mars. Nature 428, 627-630.  
675  
676 Bibring, J.-P., Langevin, Y., Mustard, J. F., Poulet, F., Arvidson, R., Gendrin, A., Gondet, B.,  
677 Mangold, N., Pinet, P., Forget, F., the OMEGA team, Berthe, M., Bibring, J.-P., Gendrin, A.,  
678 Gomez, C., Gondet, B., Jouglet, D., Poulet, F., Soufflot, A., Vincendon, M., Combes, M.,  
679 Drossart, P., Encrenaz, T., Fouchet, T., Merchiorri, R., Belluci, G., Altieri, F., Formisano, V.,  
680 Capaccioni, F., Cerroni, P., Coradini, A., Fonti, S., Korablev, O., Kottsov, V., Ignatiev, N.,  
681 Moroz, V., Titov, D., Zasova, L., Loiseau, D., Mangold, N., Pinet, P., Doute, S., Schmitt, B.,  
682 Sotin, C., Hauber, E., Hoffmann, H., Jaumann, R., Keller, U., Arvidson, R., Mustard, J. F.,  
683 Duxbury, T., Forget, F. & Neukum, G. 2006. Global Mineralogical and Aqueous Mars  
684 History Derived from OMEGA/Mars Express Data, Science 312, 400-404.  
685  
686 Bridges, N.T., Titus, T.N., Herkenhoff, K.E., Kieffer, H.H., Hecht, M.H., and Mercer, C.  
687 (2001) Seasonal dark spots in martian gullies and other terrains studied by TES and other data

688 sets. Exploring Mars with TES: A Data Users Workshop, Arizona State University, Tempe,  
689 Arizona.

690

691 Brown, A.J., Calvin, W.M., McGuire, P.C., Murchie, S.L. 2010. Compact Reconnaissance  
692 Imaging Spectrometer for Mars (CRISM) south polar mapping: First Mars year of  
693 observations. *Journal of Geophysical Research* 115, E00D13, doi:10.1029/2009JE003333.

694

695 Ceamanos, X., Douté, S., 2009. Spectral smile correction in CRISM hyperspectral images.  
696 AGU'09 - American Geophysical Union, Fall Meeting.

697

698 Christensen, P.R., Bandfield, J.L., Hamilton, V.E., Ruff, S.W.; Kieffer, H.H., Titus, T.N.,  
699 Malin, M.C., Morris, R.V., Lane, M.D., Clark, R.L., Jakosky, B.M., Mellon, M.T., Pearl, J.C.,  
700 Conrath, B.J., Smith, M.D., Clancy, R.T., Kuzmin, R.O., Roush, T., Mehall, G.L., Gorelick,  
701 N., Bender, K., Murray, K., Dason, S., Greene, E., Silverman, S., Greenfield, M., 2001. "Mars  
702 Global Surveyor Thermal Emission Spectrometer experiment: Investigation description and  
703 surface science results". *Journal of Geophysical Research* 106 (E10) 23823-23872.

704

705 Christensen, P., Anderson, D., Chase, S.C., Clark, R.N., Kieffer, H.H., Malin, M.C., Pearl,  
706 J.C., Carpenter, J.B., Nuno, B.F., 1992. Thermal emission spectrometer experiment: Mars  
707 observer mission. *Journal of Geophysical Research* 97, 7719–7734.

708

709 Christensen, P.R., Kieffer, H.H., Titus, T.N., 2005. Infrared and Visible Observations of  
710 South Polar Spots and Fans, American Geophysical Union, Fall Meeting, Abstract P23C-04.

711

712 Douté S., Schmitt, B., 1998. A multi-layer bidirectional reflectance model for the analysis of  
713 planetary surface hyperspectral images at visible and near infrared wavelengths. Journal of  
714 Geophysical Research E103:31, 367-31,390.  
715

716 Fishbaugh, K.E., Poulet, F., Chevrier, V., Langevin, Y., Bibring, J.-P., 2007. On the origin of  
717 gypsum in the Mars north polar region, Journal of Geophysical Research 112, E7, CiteID  
718 E07002.  
719

720 Forget F., Hourdin F., Fournier R., Hourdin C., Talagrand O., Collins M., Lewis S. R., Read  
721 P., Huot J.-P., 1999. Improved general circulation models of the Martian atmosphere from the  
722 surface to above 80 km. Journal of Geophysical Research 104, E10, 24155-24176.  
723

724 Forget, F., Haberle, R. M., Montmessin, F., Levrard, B., Head, J.W., 2006. Formation of  
725 Glaciers on Mars by Atmospheric Precipitation at High Obliquity. Science 311, 368-371.  
726

727 Forget, F., Millour, E., Madelaine, J., Lefevre, F., Montmessin, F., 2008. Simulation of the  
728 Mars water cycle with the LM Mars Global Climate model, The Mars water cycle workshop,  
729 Paris April 2008.  
730

731 Ganti, T., Horvath, A., Berczi, Sz., Gesztesi, A., Szathmary, E., 2003. Dark Dune Spots:  
732 possible biomarkers on mars? Origins of Life and Evolution of the Biosphere 33, 515-557.  
733

734 Grundy, W., Schmitt, B., 1998. The temperature-dependent near-infrared absorption spectrum  
735 of hexagonal H<sub>2</sub>O ice. Journal of Geophysical Research 103E, 25809-25822.  
736

737 Hansen, C., Portyankina, G., Thomas, N., Byrne, S., McEwen, A., 2010. HiRISE images of  
738 spring on Mars, 41th Lunar and Planetary Science Conference, Abstract 2029.  
739

740 Hapke, B., 2008. Bidirectional reflectance spectroscopy: 6. Effects of porosity, *Icarus* 195,  
741 918-926.  
742

743 Heinz, D., I-Chang, C., 2001. Fully constrained least squares linear spectral mixture analysis  
744 method for material quantification in hyperspectral imagery, *IEEE Transactions on*  
745 *Geoscience and Remote Sensing* 39, 529-554.  
746

747 Horvath, A., Ganti T., Gesztesi A., Berczi Sz., Szathmary E., 2001. Probable evidences of  
748 recent biological activity on Mars: appearance and growing of dark dune spots in the south  
749 polar region. 32th Lunar Planetary Science Conference. Abstract 1543.  
750

751 Horváth A., Kereszturi A., Bérczi Sz., Sik A., Pócs T., Gánti T., Szathmáry E. Analysis of  
752 Dark Albedo Features on a Southern Polar Dune Field of Mars, *Astrobiology* 9(1) 90-103.  
753

754 Kereszturi, A., Möhlmann, D., Berczi, Sz., Ganti, T., Horvath, A., Kuti, A., Sik, A. and  
755 Szathmary, E. 2010a. Indications of brine related local seepage phenomena on the northern  
756 hemisphere of Mars, *Icarus* 207, 149-164.  
757

758 Kereszturi, A., Schmidt, F., Vincendon, M., 2010. Searching for water ice in the Dark Dune  
759 Spots of Mars using CRISM data. 41th Lunar Planetary Science Conference,. Abstract 1714.  
760

761 Kereszturi A., Möhlmann D., Pócs T., Bérczi Sz., Horváth A., Sik A. 2009. Recent rheologic  
762 processes on dark polar dunes of Mars: Driven by interfacial water? *Icarus* 201, 492-503.  
763

764 Kieffer, H. H., S. C. Chase, T. Z. Martin, E. D. Miner, and F. D. Palluconi (1976), Martian  
765 north pole summer temperatures: Dirty water ice, *Science*, 194, 1341–1344,  
766 doi:10.1126/science.194.4271.1341.  
767

768 Kieffer, H. H., 1990., H<sub>2</sub>O grain size and the amount of dust in Mars' residual north polar cap,  
769 *Journal of Geophysical Research* 95(B2), 1481– 1493.  
770

771 Kieffer, H.H., 2000. Annual Punctuated CO<sub>2</sub> Slab-Ice and Jets on Mars. *International*  
772 *Conference on Mars Polar Science and Exploration* p. 93.  
773

774 Kieffer, H.H., Christensen, P.R., Titus, T.N., 2006. CO<sub>2</sub> jets formed by sublimation beneath  
775 translucent slab ice in Mars' seasonal south polar ice cap. *Nature* 442, 793-796.  
776

777 Kieffer, H.H., Titus, T.N. Mullins, K.F., and Christensen, P.R. (2000) Mars south polar spring  
778 and summer behaviour observed by TES: seasonal cap evolution controlled by frost grain  
779 size. *J. Geophys. Res.* 105:9653–9700.  
780

781 Kieffer, H.H., Titus, T.N., 2001. TES mapping of Mars' north seasonal cap. *Icarus* 154,  
782 162–180.  
783

784 Kieffer, H.H. (2003) Behaviour of CO<sub>2</sub> on Mars: real zoo [abstract 3158]. In 6th International  
785 *Conference on Mars, Lunar and Planetary Institute, Houston.*

786

787 Kossacki, K.J., Markiewicz, W.J., Portyankina, G., Neukum, G., HRSC team., 2006.

788 Conditions for water ice accumulation within craters on Mars. 4th Mars Polar Science

789 Conference, Abstract 8016.

790

791 Kossacki, J.K., Kopystynski, L., 2004. Non-uniform seasonal defrosting of subpolar dune

792 filed on Mars. *Icarus* 168, 201-204.

793

794 Langevin, Y., Poulet, F., Bibring, J.-P., Gondet, B., 2005. Sulfates in the North Polar Region

795 of Mars Detected by OMEGA/Mars Express, *Science* 307, 1584-1586

796

797 Langevin, Y., Bibring, J.P., Douté, S., Vincendon, M., Poulet, F., Gondet, B., Schmitt, B.,

798 Forget, F., Montmessin, F., and the OMEGA Team, 2006. CO<sub>2</sub> ice and H<sub>2</sub>O ice in

799 the seasonal caps of Mars during the spring retreat, phase. In: 4th Mars Polar Sci. Conf.

800 Abstract 8091.

801

802 Langevin, Y., Bibring, J.-P., Montmessin, F., Forget, F., Vincendon, M., Doute, S., Poulet, F.,

803 Gondet, B., 2007. Observations of the south seasonal cap of Mars during recession in 2004–

804 2006 by the OMEGA visible/near-infrared imaging spectrometer on board Mars Express.

805 *Journal of Geophysical Research* 112, E08S12, doi:10.1029/2006JE002841.

806

807 Langevin, Y., Vincendon, M., Poulet, F., Bibring, J.-P., Gondet, B., Douté, S., Encrenaz, T.,

808 2008. Weak Signatures of Water Ice at High Northern Latitudes: Aerosols, Frosts and Ice

809 Outcrops, 39th Lunar and Planetary Science Conference, Abstract 2134.

810

811 Malin, M.C., Carr, M.H., Danielson, G.E., Davies, M.E., Hartmann, W.K., Ingersoll, A.P.,  
812 James, P.B., Masursky, H., McEwen, A.S., Soderblom, L.A., Thomas, P., Veverka, J.,  
813 Caplinger, M.A., Ravine, M.A., Soulanille, T.A., Warren, J.L., 1998. Early Views of the  
814 Martian Surface from the Mars Orbiter Camera of Mars Global Surveyor. *Science* 279, 1681–  
815 1685.

816

817 Malin, M.C., Edgett, K.S., 2000. Frosting and defrosting of Martian polar dunes, 31th Lunar  
818 Planetary Science Conference., Abstract 1056.

819

820 Malin, M.C. and Edgett, K.S. (2001) The Mars Global Surveyor Mars Orbiter camera:  
821 interplanetary cruise through primary mission. *J. Geophys. Res.* 106:23429–23570.

822

823 Massé, M., Bourgeois, O., Le Mouélic, S., Verpoorter, C. & Le Deit, L., 2010. Origin of  
824 Martian Circum-Polar Gypsum-bearing Deposits, 41th Lunar and Planetary Science  
825 Conference, Abstracts 1138.

826

827 McGuire, P.C., Bishop, J.L., Brown, A.J., Fraeman, A.A., Marzo, G.A., Morgan, M.F.,  
828 Murchie, S.L., Mustard, J.F., Parente, M., Pelkey, S.M., Roush, T.L., Seelos, F.P., Smith,  
829 M.D., Wendt, L., Wolff, M.J., 2009. An improvement to the volcano-scan algorithm for  
830 atmospheric correction of CRISM and OMEGA spectral data. *Planetary and Space Science*  
831 57, 809-815.

832

833 Mohlmann, D., 2004. Water in the upper martian surface at mid- and low-latitudes: presence,  
834 state, and consequences. *Icarus* 168. 318-323.

835

836 Mohlmann, D., 2009. Temporary liquid water in upper snow/ice sub-surfaces on Mars? *Icarus*  
837 207, 140-148.  
838  
839 Mohlmann, D., 2010. The three types of liquid water in the surface of present Mars.  
840 *International Journal of Astrobiology* 9/1. 45-49.  
841  
842 Möhlmann D., Kereszturi A. Viscous liquid film flow on dune slopes of Mars, *Icarus* 207,  
843 654-658. doi:10.1016/j.icarus.2010.01.002  
844  
845 Montmessin, F., Forget, F., Rannou, P., Cabane, M. and R. M. Haberle. Origin and role of  
846 water ice clouds in the Martian water cycle as inferred from a general circulation model.  
847 *Journal of Geophysical Research* 109, E10, doi:10.1029/2004JE002284, 2004  
848  
849 Morgan, F., Seelos, F., Murchie, S., 2009. CAT Tutorial, presentation at the CRISM  
850 Workshop The Woodlands, TX.  
851  
852 Murchie, S., Arvidson, R., Bedini, P., Beisser, K., Bibring, J.-P., Bishop, J., Boldt, J.,  
853 Cavender, P., Choo, T., Clancy, R. T., Darlington, E.H., Des Marais, D., Espiritu, R., Fort, ,  
854 Green, R., Guinness, E., Hayes, J., Hash, C., Heffernan, K., Hemmler, J., Heyler, G., Humm,  
855 D., Hutcheson, J., Izenberg, N., Lee, R., Lees, J., Lohr, D., Malaret, E., Martin, T.,  
856 McGovern, J.A., McGuire, P., Morris, R., Mustard, J., Pelkey, S., Rhodes, E., Robinson, M.,  
857 Roush, T., Schaefer, E., Seagrave, G., Seelos, F., Silverglate, P., Slavney, S., Smith, M.,  
858 Shyong, W.-J., Strohbahn, K., Taylor, H., Thompson, P., Tossman, B., Wirzburger, M.,  
859 Wolff, M., 2007. Compact Reconnaissance Imaging Spectrometer for Mars (CRISM) on Mars

860 Reconnaissance Orbiter (MRO). *Journal of Geophysical Research* 112, E05S03,  
861 doi:10.1029/2006JE002682.

862

863 Ness, P.K., Orme, G.M., 2002. Spider-ravine models and plant-like features on Mars -  
864 Possible geophysical and biogeophysical modes of origin. *Journal of the British Interplanetary*  
865 *Society* 55 (3-4): 85-108.

866

867 Pelkey, S.M., Mustard, J.F., Murchie, S., Clancy, R.T., Wolff, M., Smith, M., Milliken, R.,  
868 Bibring, J.-P., Gendrin, A., Poulet, F., Langevin, Y., Gondet, B., 2007. CRISM multispectral  
869 summary products: Parameterizing mineral diversity on Mars from reflectance. *Journal of*  
870 *Geophysical Research* 112, E08S14, doi:10.1029/2006JE002831.

871

872 Parente, M., 2008. A new approach to denoising CRISM images. 39th Lunar and Planetary  
873 *Science Abstract* 2528.

874

875 Piqueux, S., Byrbe, S., Richardson, M.I., 2003. Sublimation of Mars's Southern seasonal CO<sub>2</sub>  
876 ice cap and the formation of spiders. *Journal of Geophysical Research* 108, 5084.

877

878 Pocs, T., Horvath, A., Ganti, T., Berczi, Sz., Szathmary E., 2003. Are the Dark Dune Spots  
879 Remnants of the Crypto-Biotic-Crust of Mars? Vernadsky/Brown Microsymposium on  
880 *Comparative Planetology* 38.

881

882 Rennó, N.O., Bos, B.J., Catling, D., Clark, B.C., Drube, L., Fisher, D., Goetz, W., Hviid,  
883 S.,F., Keller, H.U., Kok, J.F., Kounaves, S.P., Leer, K., Lemmon, M., Madsen, M.B.,  
884 Markiewicz, W.J., Marshall, J., McKay, C., Mehta, M., Smith, M., Zorzano, M.P.; Smith,

885 P.H., Stoker, C., Young, S.,M.M., 2009a. Possible physical and thermodynamical evidence  
886 for liquid water at the Phoenix landing site. *Journal of Geophysical Research* 114, C10,  
887 CiteID E00E03.  
888

889 Rennó, N.O., Mehta, M., Block, B.P., Braswell, S., 2009b. The discovery of liquid water on  
890 Mars and its implications for astrobiology. *Instruments and Methods for Astrobiology and*  
891 *Planetary Missions XII. Proceedings of the SPIE, Volume 7441, 74410C-74410C-12.*  
892

893 Reiss, D., Erkeling, G., Bauch, K.E., Hiesinger, H. 2010. Evidence for present day gully  
894 activity on the Russell crater dune field, Mars. *Geophysical Research Letters* 37, L06203,  
895 doi:10.1029/2009GL042192.  
896

897

898

899

900 Schmidt, F.; Douté, S.; Schmitt, B.; Vincendon, M.; Bibring, J.-P.; Langevin, Y. & the  
901 OMEGA Team 2009, Albedo control of seasonal South Polar cap recession on Mars, *Icarus*  
902 200, 374-394, doi: 10.1016/j.icarus.2008.12.014  
903

904 Schmidt, F.; Schmitt, B.; Douté, S.; Forget, F.; Jian, J.-J.; Martin, P.; Langevin, Y.; Bibring,  
905 J.-P. & the OMEGA Team 2010, Sublimation of the Martian CO<sub>2</sub> Seasonal South Polar Cap  
906 *Planetary and Space Science* 58, 1129-1138, DOI: 10.1016/j.pss.2010.03.018.  
907

908 Schmitt, B., Quirico, E., Trotta, F. & Grundy, W. M., Schmitt, B., de Bergh, C. & Festou, M.  
909 (ed.), *Optical Properties of Ices from UV to Infrared*, Solar System Ices, Kluwer, 1998, 227,  
910 199-240.

911

912 Schmitt, B., Douté, S., Langevin, Y., Forget, F., Bibring, J.P., Gondet, B., and the OMEGA  
913 Team, 2005. Northern seasonal condensates on Mars by Omega/Mars Express.  
914 *Lunar Planet. Sci.* 6. Abstract 2326

915

916 Schmitt, B., Schmidt, F., Douté, S., Langevin, Y., Forget, F., Bibring, J.P., Gondet, B.,  
917 and the OMEGA Team, 2006. Recession of the northern seasonal condensates on Mars by  
918 OMEGA/Mars Express. In: *4th Mars Polar Sci. Conf.* Abstract 8050.

919

920 Schmitt, B., Appéré, T., Douté, S., Beck, P., Forget, F., Langevin, F. Y. Bibring, J.-P. 2009.  
921 Microphysical cycle of evolution of the northern Martian seasonal condensates. Third  
922 International Workshop on Mars Polar Energy Balance and the CO<sub>2</sub> Cycle, abstract 7027.

923

924 Shkuratov, Y., Starukhina, L., Hoffmann, H. Arnold, G., 1999. A Model of Spectral Albedo  
925 of Particulate Surfaces: Implications for Optical Properties of the Moon, *Icarus* 137, 235-246.

926

927 Szathmary, E., Ganti, T., Pocs, T., Horvath A., Kereszturi, A., Berczi, Sz. and Sik, A., 2007.  
928 Life in the dark dune spots of Mars: a testable hypothesis - in *Planetary Systems and the*  
929 *Origin of Life*, ed. Ralph Pudritz, Paul Higgs, Jonathan Stone, Cambridge University Press,  
930 pp. 241-262.

931

932 Titus, Timothy N.; Kieffer, Hugh H.; Christensen, Phillip R., 2003. Exposed Water Ice  
933 Discovered near the South Pole of Mars. *Science*, Volume 299, Issue 5609, pp. 1048-1051.  
934  
935 Titus, T.N., 2005. Thermal infrared and visual observations of a water ice lag in the  
936 Mars southern summer. *Geophys. Res. Lett.* 32 (24), doi:10.1029/2005GL024211. L24204.  
937  
938 Titus, T.N., Kieffer, H.H., Langevin, Y., Murchie, S., Seelos, F., Vincendon, M., 2007, Bright  
939 Fans in Mars Cryptic Region Caused by Adiabatic Cooling of CO<sub>2</sub> Gas Jets. American  
940 Geophysical Union, Fall Meeting, Abstract #P24A-05.  
941  
942 Titus, T., 2008. Infrared observations of Mars south polar water ice. In: Mars Water Cycle  
943 Workshop, Paris.  
944  
945 Vincendon, M., Langevin, Y., Poulet, F., Bibring, J.-P., Gondet, B., 2007. Recovery of  
946 surface reflectance spectra and evaluation of the optical depth of aerosols in the near-IR using  
947 a Monte Carlo approach: Application to the OMEGA observations of high-latitude regions of  
948 Mars. *Journal of Geophysical Research* 112, E08S13, doi:10.1029/2006JE002845.  
949  
950 Vincendon, M., Mustard, J., Forget, F., Kreslavsky, M., Spiga, A., Murchie, S., Bibring, J.-P.,  
951 2010. Near-tropical subsurface ice on Mars. *Geophysical Research Letters* 37, L01202,  
952 doi:10.1029/2009GL041426.  
953  
954 Vincendon, M., Forget, F., Mustard, J. 2010. Water ice at low to mid latitudes on Mars,  
955 *Journal of Geophysical Research*, doi:10.1029/2010JE003584, in press.  
956

957 Wagstaff, K.L., Titus, T.N., Ivanov, A.B., Castaño, R., Bandfield, J.L. 2008. Observations of  
958 the north polar water ice annulus on Mars using THEMIS and TES. Planetary and Space  
959 Science 56. 256-265.

960

961 Zuber, M.T., 2003. Learning to think like Martians. Science 302, 1694-1695.

962

963

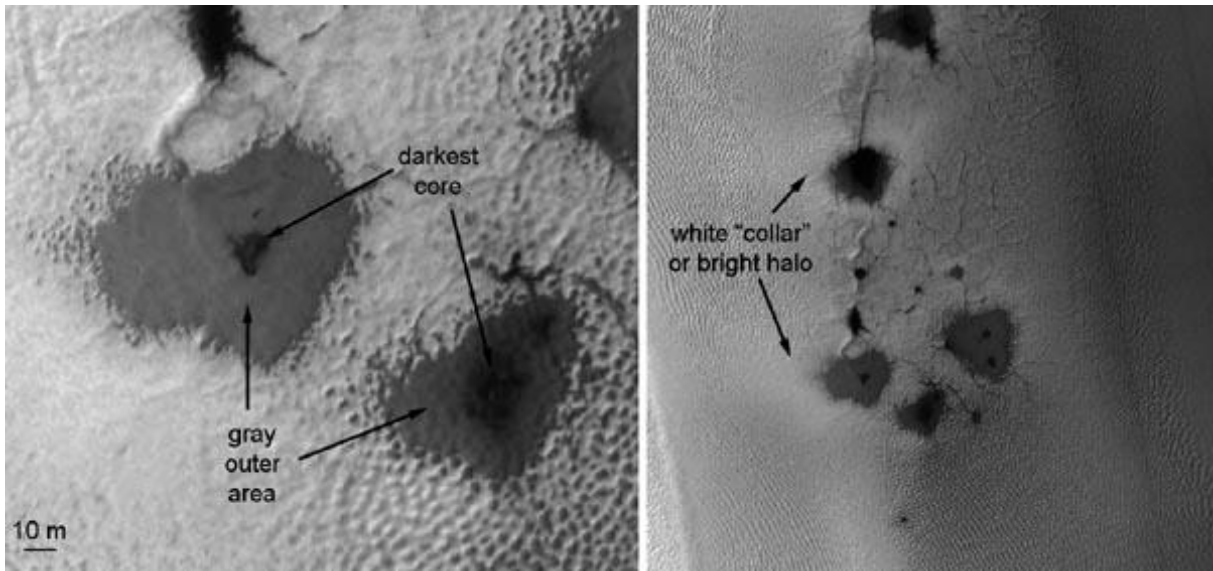
964 Figure captions

965

966 Fig. 1. The analyzed unit types of the spots in Richardson crater on the HiRISE image #

967 PSP\_003175\_1080. Dark cores and gray outer rings are visible in the left subset, while

968 elongated and probably wind blown bright halos are present in the right subset.



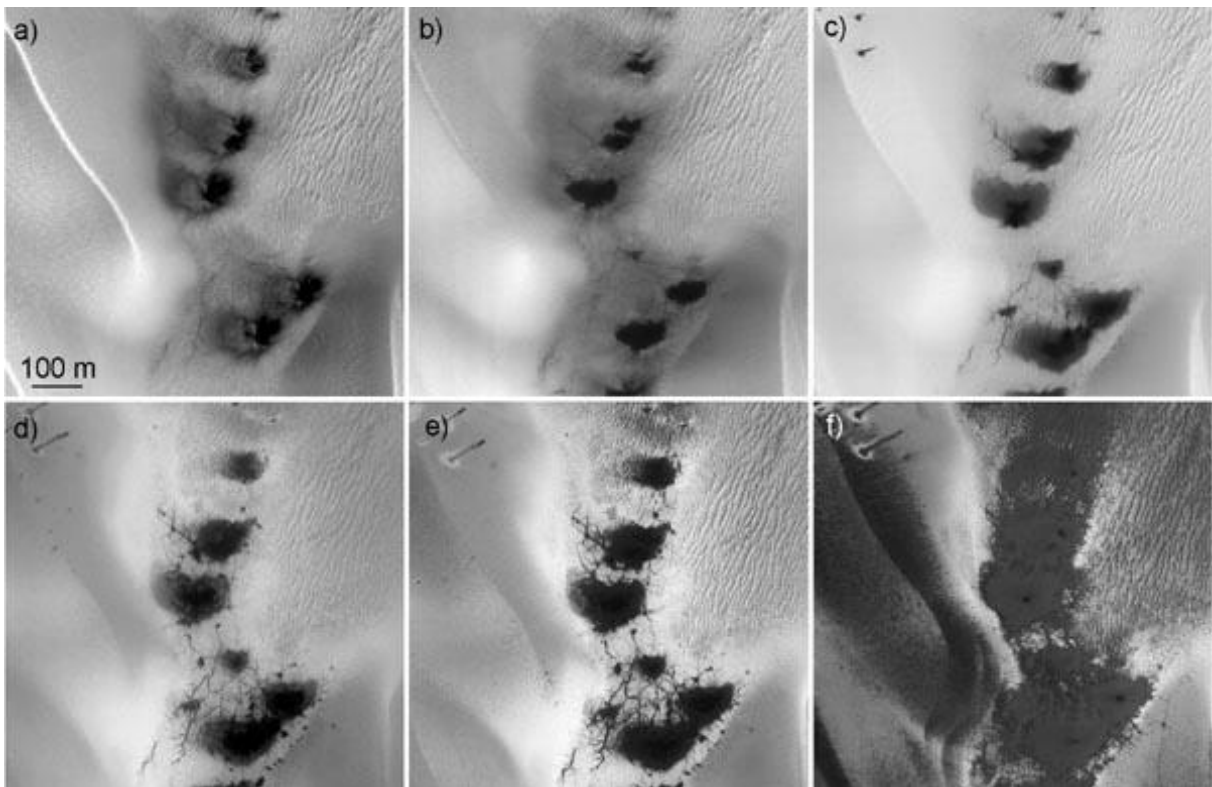
969

970

971

972

973 Fig. 2. Sequence of HiRISE images showing the temporal change of the same terrain with  
974 Dark Dune Spots in Richardson crater. At the earliest phase (a, b) only dark cores are present  
975 and wind blown dark streaks emanate from them toward the left, later the continuous gray  
976 ring forms around the dark cores (c, d), even later dark cores are expanding and gray rings  
977 contracting (d,e), finally only albedo differences are visible (f) but no ice is present based on  
978 CRISM data (image number and solar longitude values are: a) PSP\_002186\_1080 ( $L_S=166.2$ ),  
979 b) PSP\_002397\_1080 ( $L_S=172.5$ ), c) PSP\_002885\_1080 ( $L_S=197.0$ ), d) PSP\_003597\_1080  
980 ( $L_S=230.9$ ), e) PSP\_003742\_1080 ( $L_S=238.1$ ), f) PSP\_003953\_1080 ( $L_S=248.1$ )).

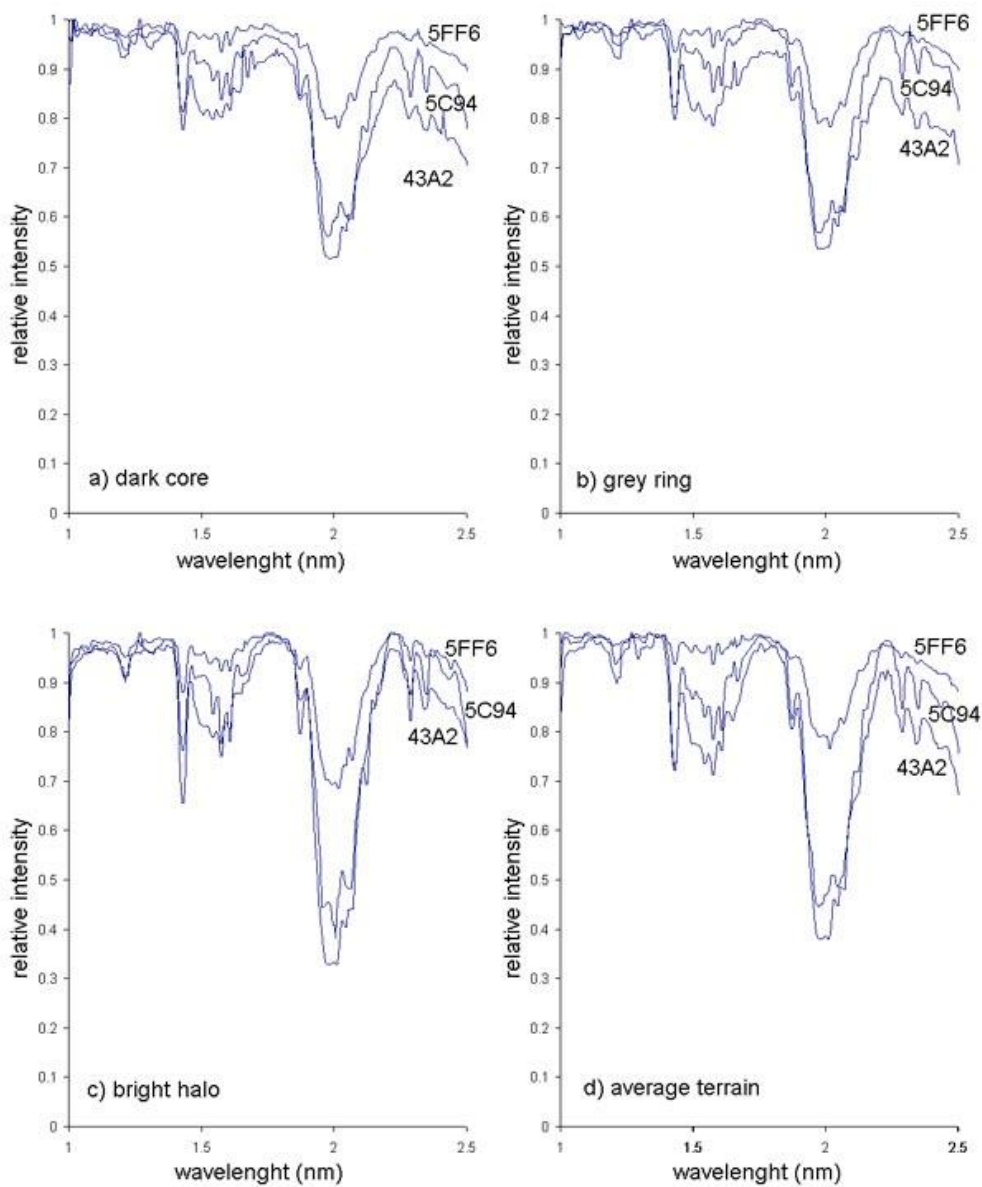


981

982

983

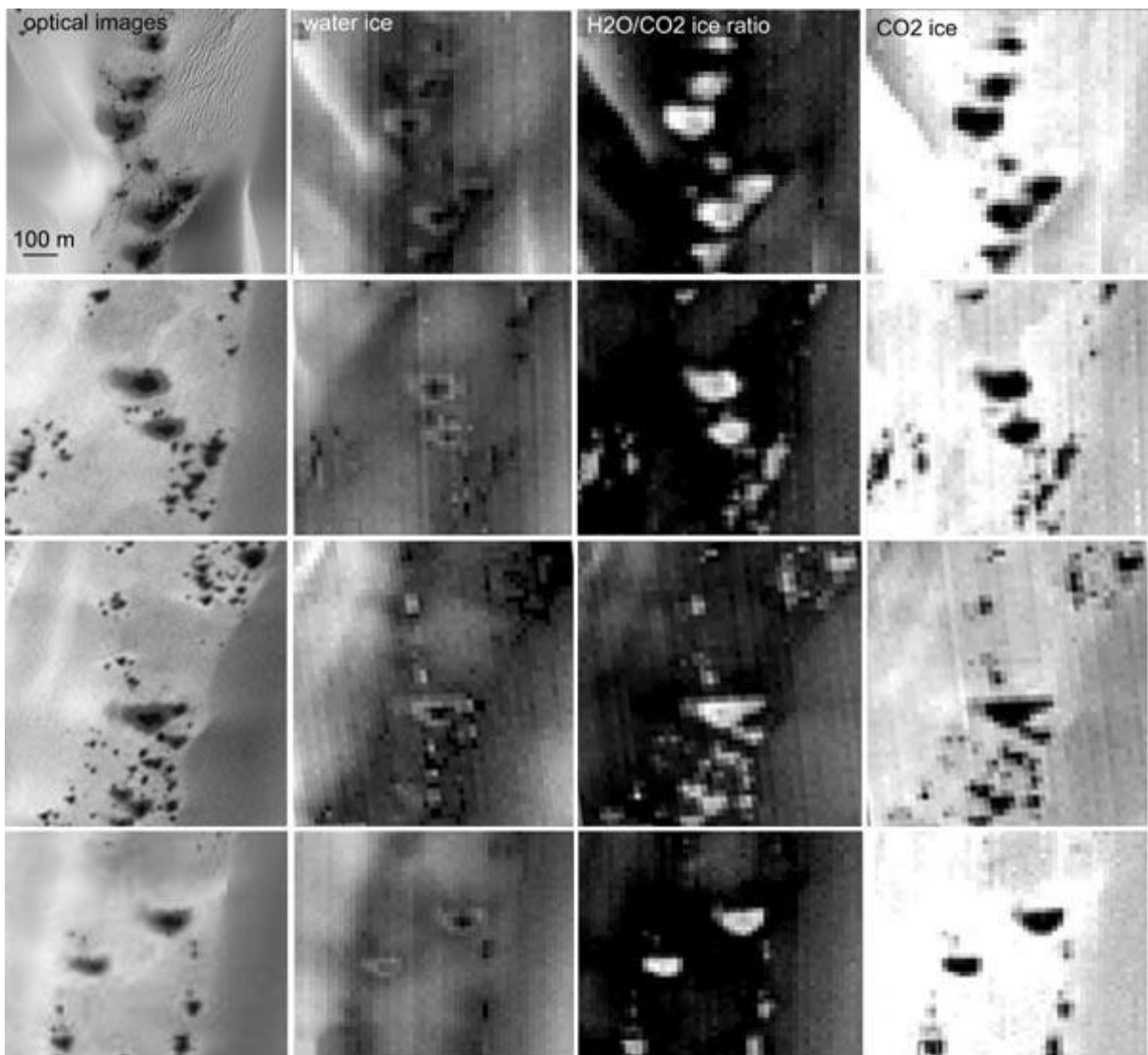
984 Fig. 3. Spectral shapes for three different periods (on images: 43a2, 5C94, 5FF6 at  $L_S=181.7,$   
985 242.7, 248.7), marked with black, gray and light gray color) for the analyzed surface units  
986 (dark centre, gray ring, bright halo, undisturbed ice), normalized to the continuum, between  
987 1.0 and 2.6 micrometer. Carbon-dioxide and water ice signatures are present with decreasing  
988 band depth as the season progresses.



989

990

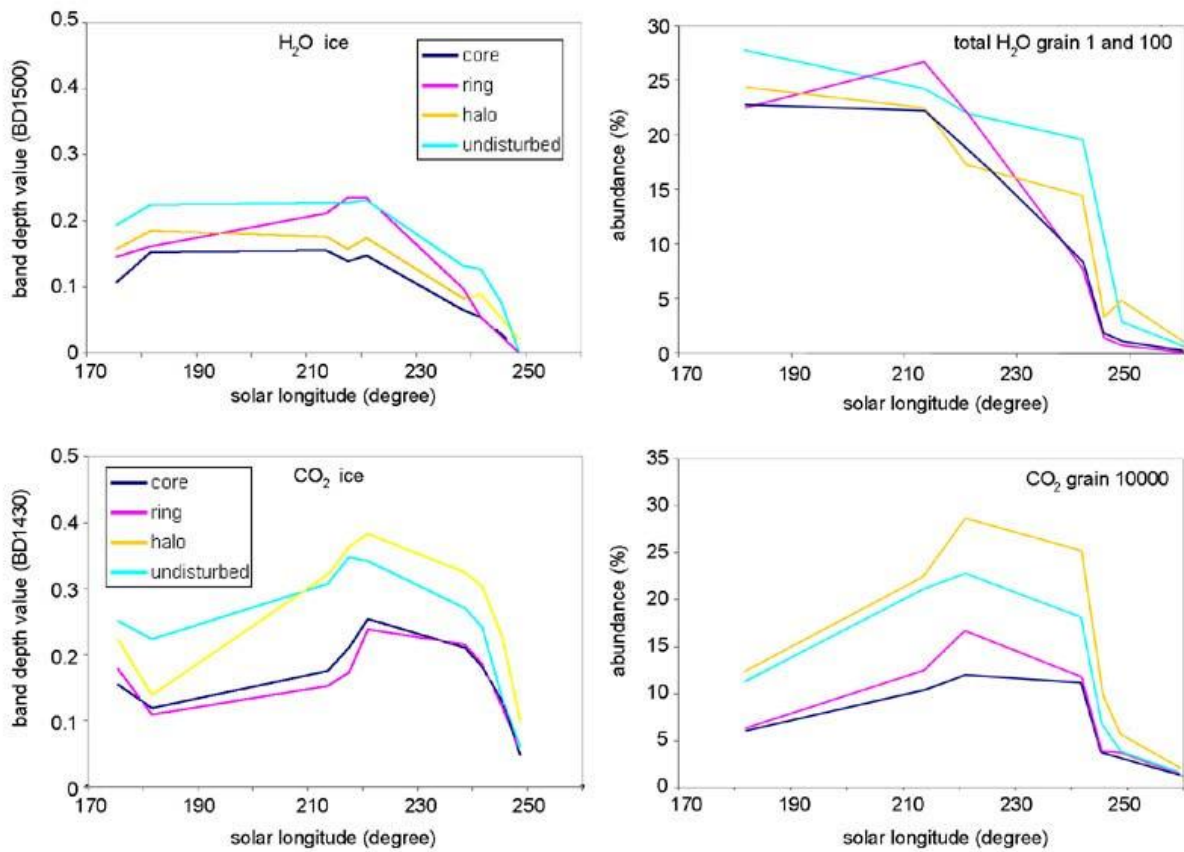
991 Fig. 4. Comparison of the distribution of water and CO<sub>2</sub> ice. The different rows show different  
992 locations in Richardson crater, and different columns are for: optical images  
993 (PSP\_00307\_1080 Column #1), water ice band depth image (BD1500 Column #2), image  
994 representing the ratio of H<sub>2</sub>O/CO<sub>2</sub> ice (inverted ICER1 band Column #3), and CO<sub>2</sub> ice band  
995 depth images (BD1430 Column #4). The bright water ice rings in column #2 suggest surface  
996 H<sub>2</sub>O ice is present in the gray ring unit.



997

998

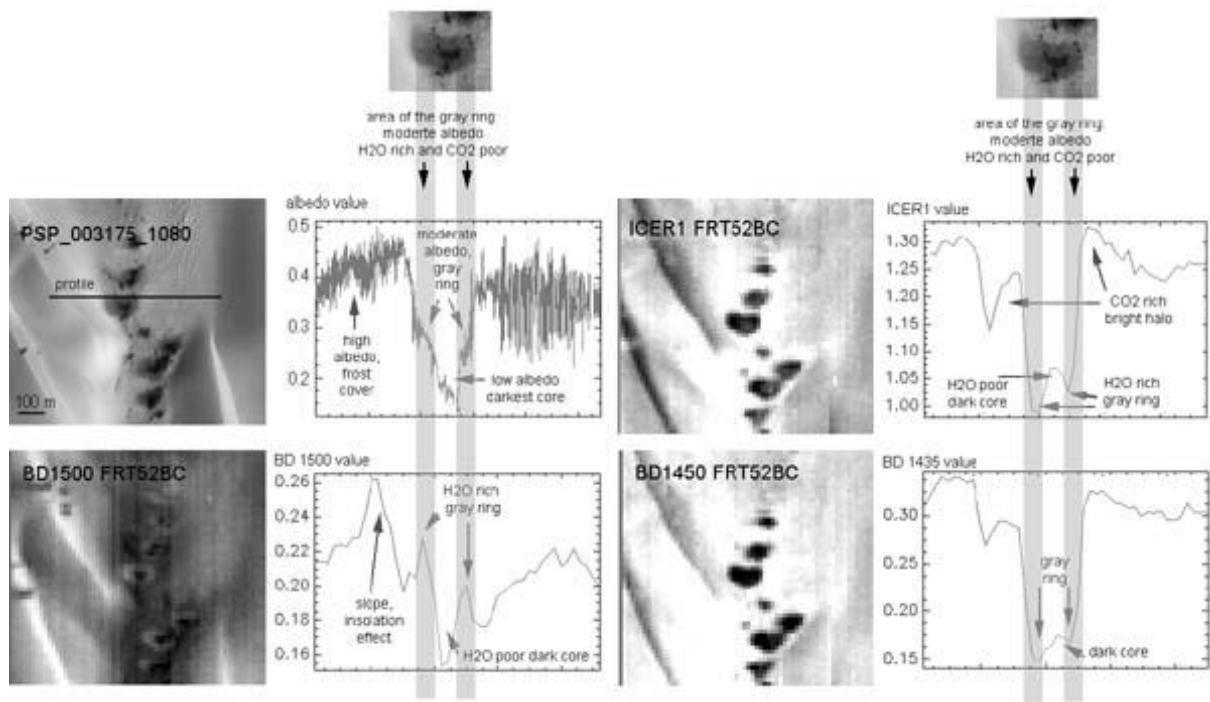
999 Fig. 5. Temporal changes of H<sub>2</sub>O and CO<sub>2</sub> ice related band depth values (on left) and spectral  
 1000 abundances estimated with the linear unmixing method FCLS (on right, see fig. 12 for more  
 1001 detailed explanation) for different units (core: blue, ring: pink, halo: yellow, undisturbed ice:  
 1002 blue). The top right panel shows the sum of the abundances of water ice at different grain size  
 1003 (only grain size of 1 and 100 microns are detected). The bottom right panel shows the  
 1004 abundance of CO<sub>2</sub> ice (only at 10 cm grain size). Top: H<sub>2</sub>O ice. A general decrease can be  
 1005 seen, except for the gray ring, where an increase is present about Ls 215°. Bottom: CO<sub>2</sub> ice.  
 1006 The amount of CO<sub>2</sub> ice increases during early spring, with a stronger increase seen during the  
 1007 formation of the bright halo feature (yellow).



1008

1009

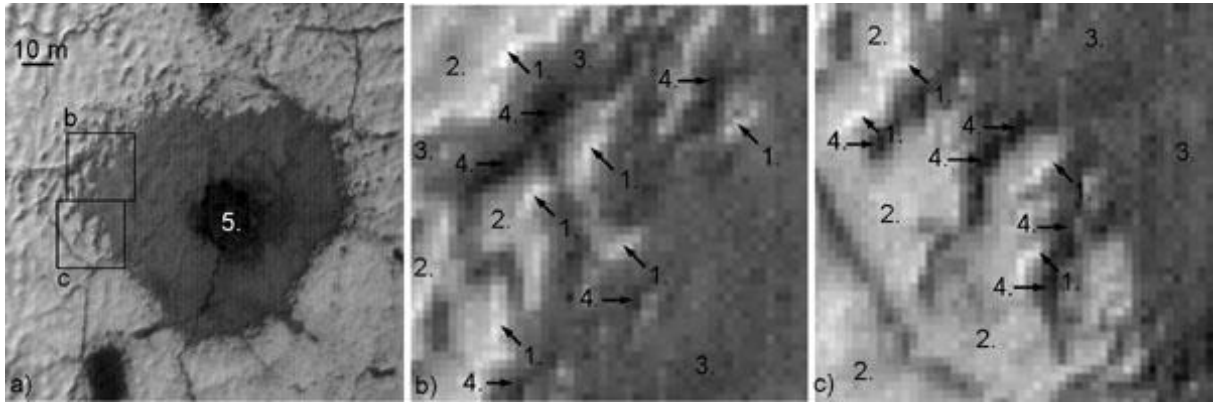
1010 Fig. 6. Spatial changes on images (left) and graphs (right) along a spot for different  
 1011 parameters: a) albedo (HiRISE), b) water ice (BD1500), c) ratio of CO<sub>2</sub>/H<sub>2</sub>O ice (ICER1) and  
 1012 d) CO<sub>2</sub> ice (BD1430). The two gray columns on the right mark the location of the gray ring  
 1013 (R) area along the profile, showing a decreased CO<sub>2</sub> ice signature and an increased H<sub>2</sub>O ice  
 1014 signature at this location. The magnified image of the analyzed spot is visible at the top right.  
 1015 The subsets show that the lowest albedo is found in the core (C), which is H<sub>2</sub>O ice poor and  
 1016 shows some CO<sub>2</sub> ice signature (from atmospheric dust scattering of outer surfaces and/or  
 1017 from the surface). The outer ring (R) corresponds to a local minima in albedo with an elevated  
 1018 H<sub>2</sub>O ice signature a low CO<sub>2</sub> ice signature. The high CO<sub>2</sub> signature of the bright halo (H) and  
 1019 the average frost covered terrain (F) is also marked, while slope effect (SE) is indicate the  
 1020 elevated value by a solar facing large slope.



1021

1022

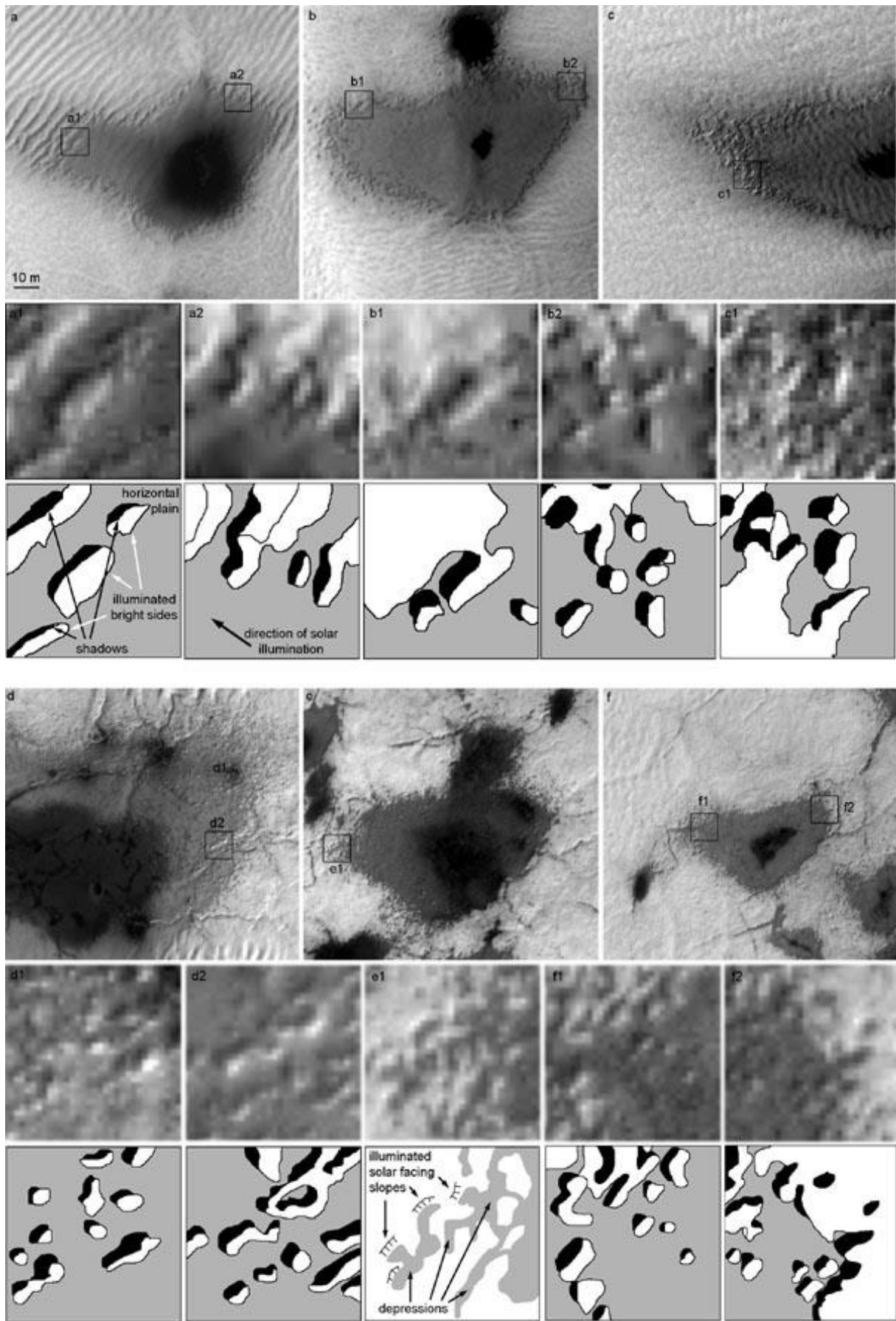
1023 Fig. 7. Estimation of the topographic heights from shadow measurements (HiRISE image  
1024 PSP\_003175\_1080). Five units are distinguished on the basis of their brightness (from 1 to 5).  
1025 The context image a) shows a Dark Dune Spots with the locations of the magnified b) and c)  
1026 subsets. In these subsets numbers arrows point toward examples for 4 of the 5 different units,  
1027 while the darkest unit # 5 can be seen in the main image (a).



1028

1029

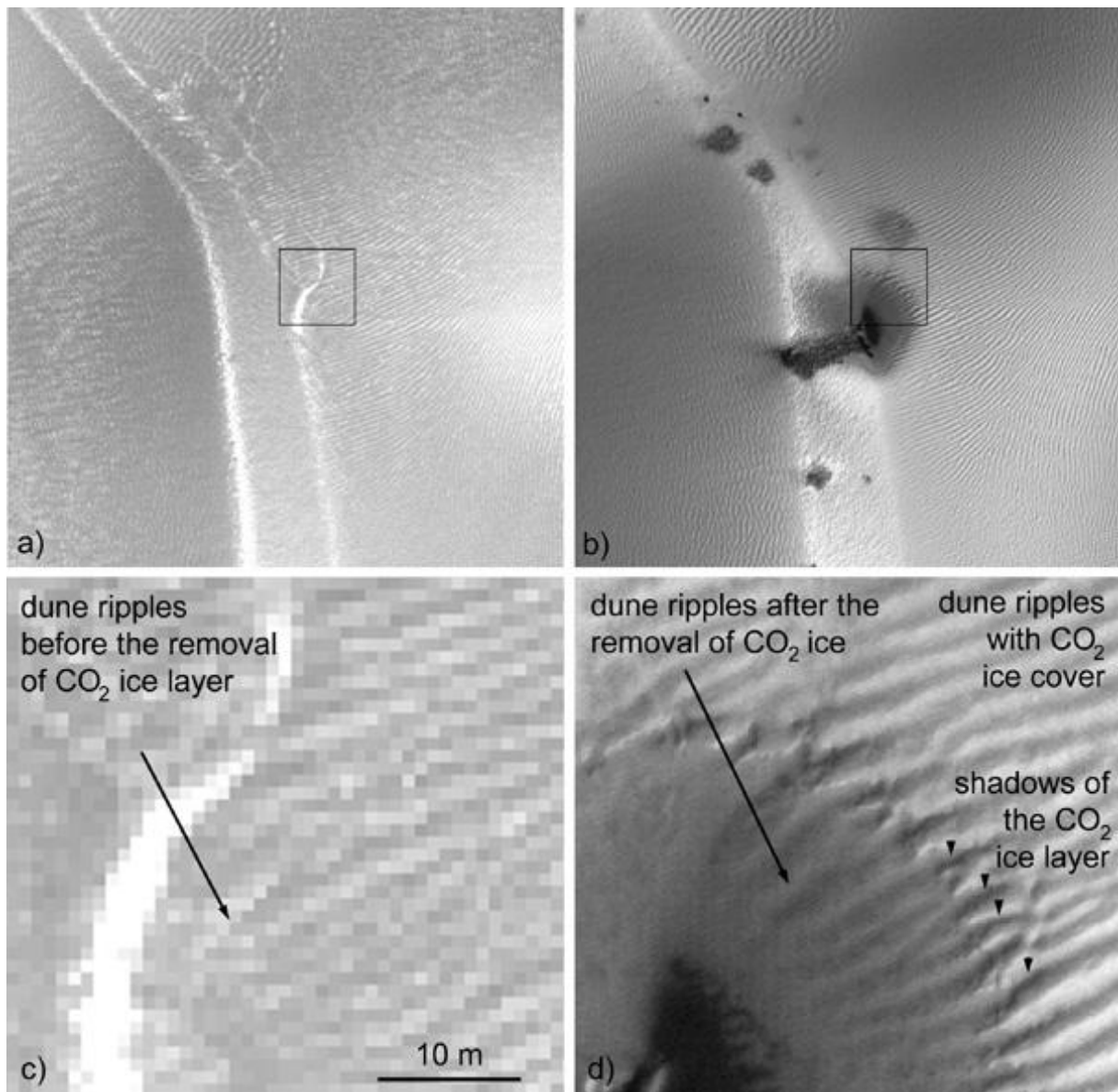
1030 Fig. 8. Examples for the disappearing bright layer forming the depressed gray ring on the  
1031 HiRISE image no. PSP\_003175\_1080. Six large spots are shown (largest images labeled a, b,  
1032 c, d, e, f). Ten insets (10x10 m) from these images are extracted (a1, a2, b1, b2, c1, d1, d2, e1,  
1033 f1, f2). Outlines of these 10 insets have been produced to highlight the main features and the  
1034 shadows. In the small inset images the bright ice layer casts shadows, somewhere shadow are  
1035 present behind iceberg like heights. The Sun illuminates from the lower right, shadows are  
1036 elongated to the upper left. The outlines show the solar facing and brighter slopes with white,  
1037 the opposite slopes in shadow with dark, and the nearly horizontal plains (between or on the  
1038 top of the heights composed of CO<sub>2</sub> ice) with gray color.



1039

1040

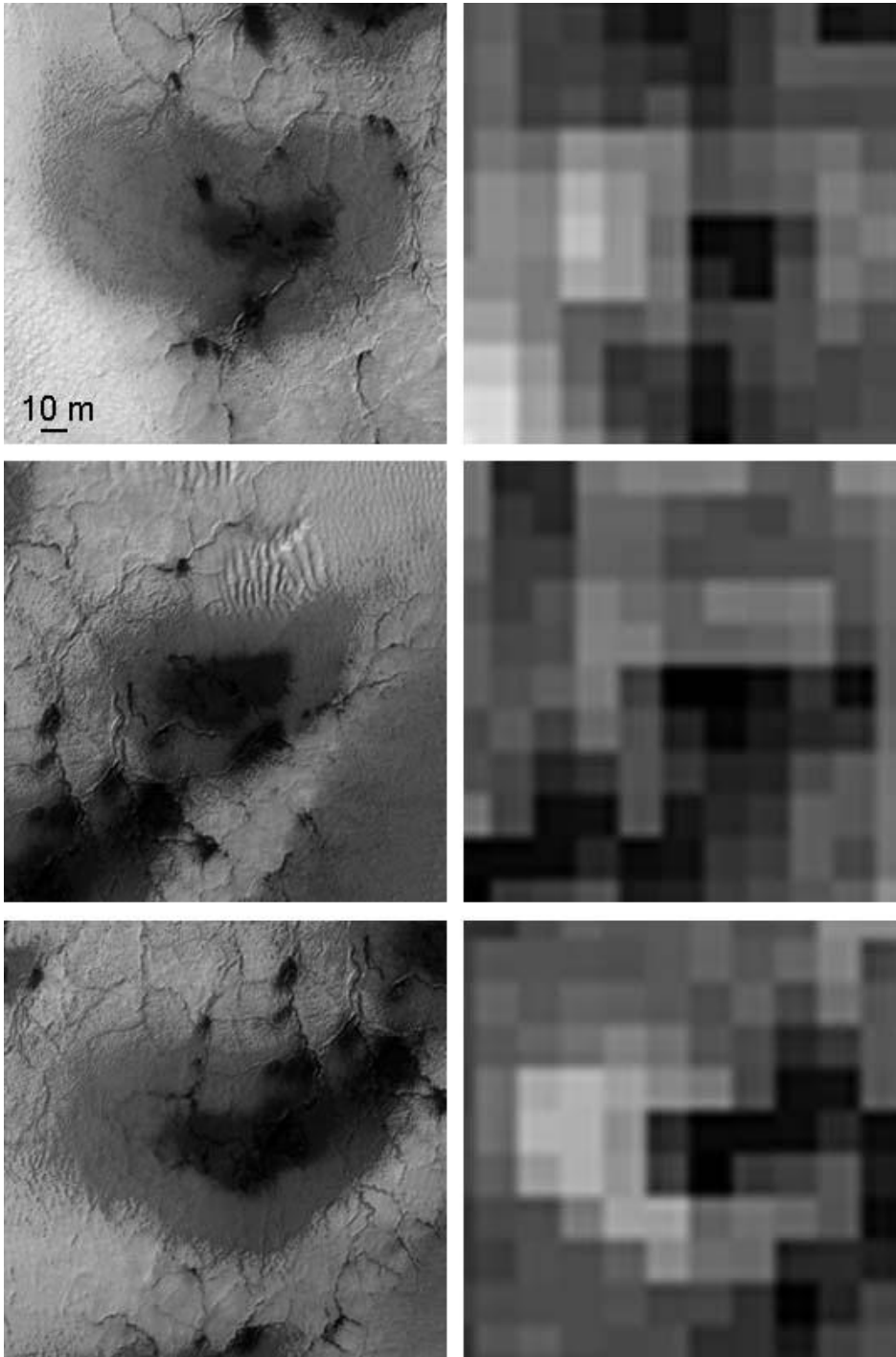
1041 Fig. 9. An example area before and after the development of a spot in Richardson crater. The  
1042 a) and b) image PSP\_002252\_1080 and PSP\_003175\_1080 were acquired at Ls=169.0, 210.6  
1043 respectively. The same small boxed areas are extracted below in c) and d) subsets. It can be  
1044 seen that the depression of the gray ring (b, d) was not present earlier (a, c), in the previously  
1045 CO<sub>2</sub> ice covered area. Small dune ripples are present in the CO<sub>2</sub> ice covered and CO<sub>2</sub> ice free  
1046 area also. In subset d) the surface topography may contribute in producing the shadows, but  
1047 the image suggests CO<sub>2</sub> ice contributed alone substantially in making the shadows, , as it also  
1048 can be seen from isolated CO<sub>2</sub> ice heights in Fig. 8.



1049

1050

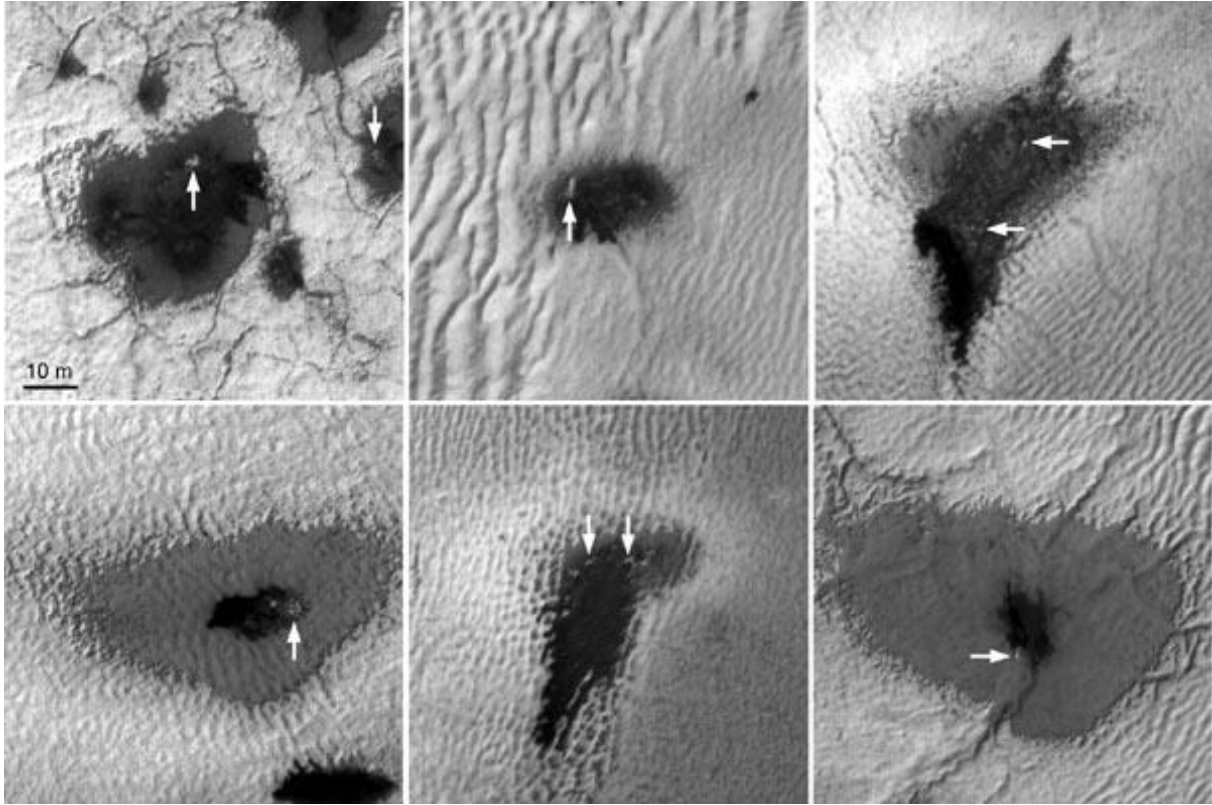
1051 Fig. 10. Three examples for the spatial correlation between HiRISE image insets (left, from  
1052 PSP\_003175\_1080 HiRISE image) and BD1500 values (right) from the CRISM image insets  
1053 (FRT000052BC\_07\_IF163L). Despite the difference in spatial resolution we can see that the  
1054 location of the strong BD1500 values (bright pixels on the right) coincide with the gray ring  
1055 area (on the left).



1056

1057

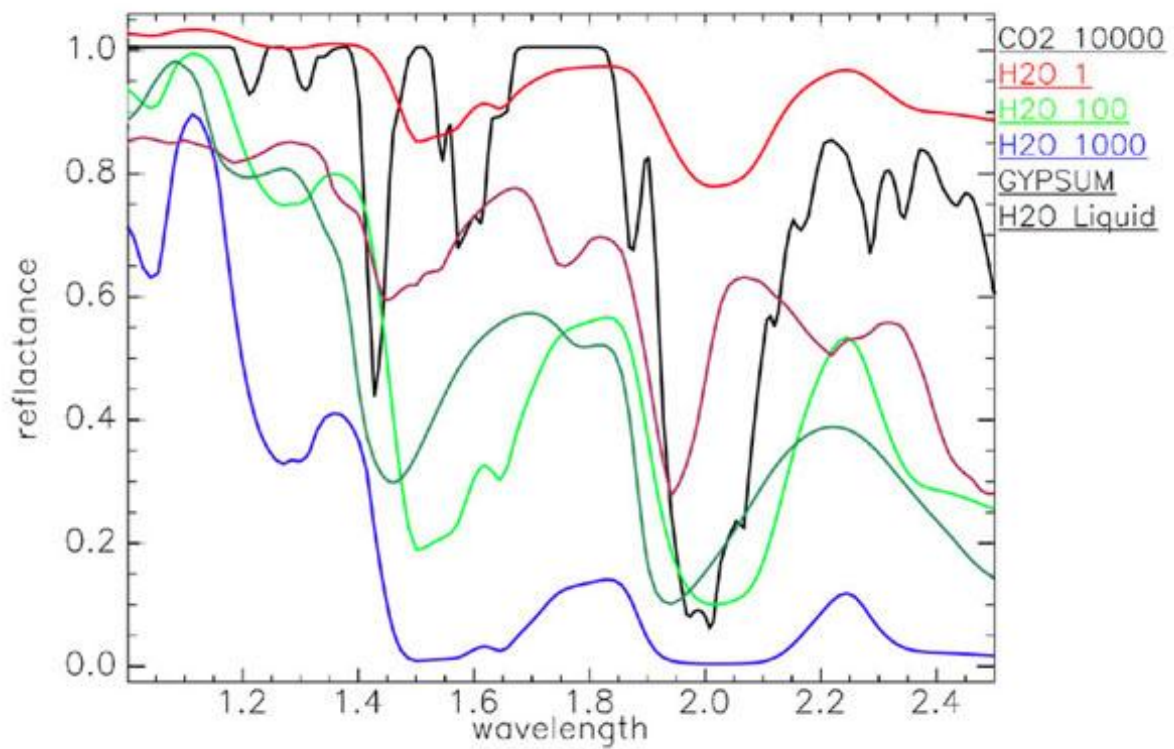
1058 Fig. 11. Examples for small bright patches inside the spots (arrows) on HiRISE image  
1059 PSP\_003386\_1080. These suggest, small CO<sub>2</sub> ice patches may still be present even at the  
1060 darkest cores, which are below the spatial resolution of CRISM data, but may effect the  
1061 spectra.



1062

1063

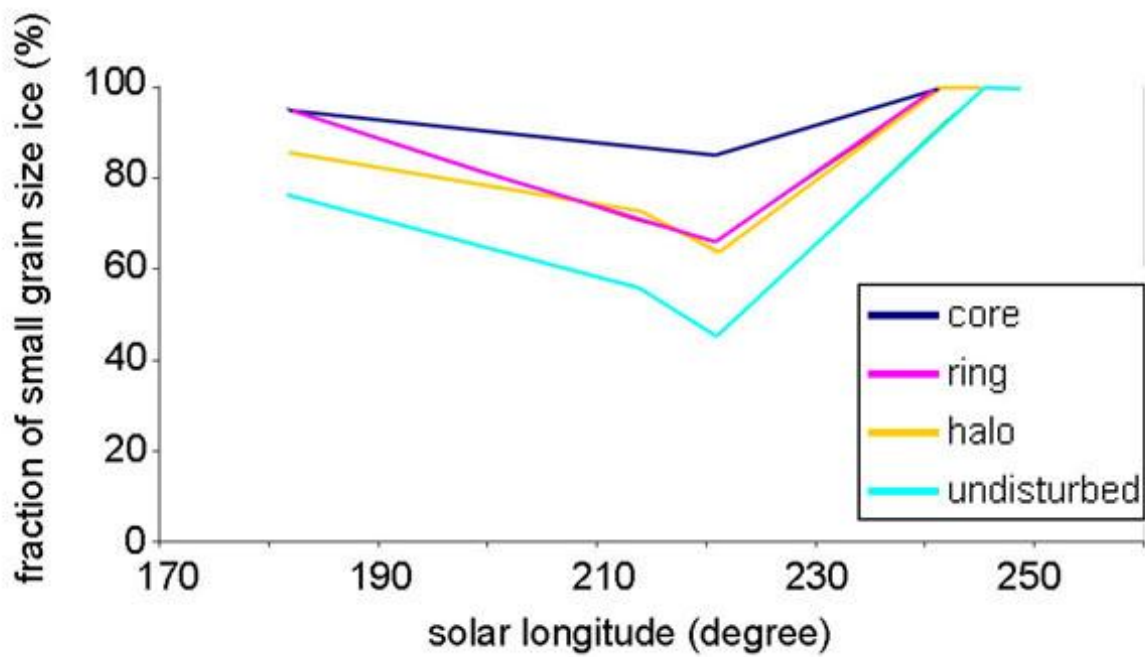
1064 Fig. 12. Reference spectra used by FCLS to estimate the relative abundances for observed  
1065 CRISM spectra. CO<sub>2</sub> ice at 10 cm grain size, H<sub>2</sub>O ice at 1, 100 and 1000 microns have been  
1066 modeled by a radiative transfer code (Douté and Schmitt, 1998) using optical constant  
1067 recorded in the laboratory (Schmitt et al., 1998). Both gypsum and liquid water have been  
1068 acquired at LPG (Schmitt and Pommerol, unpublished). These spectra will be soon available  
1069 online at <http://ghosst.obs.ujf-grenoble.fr>.



1070

1071

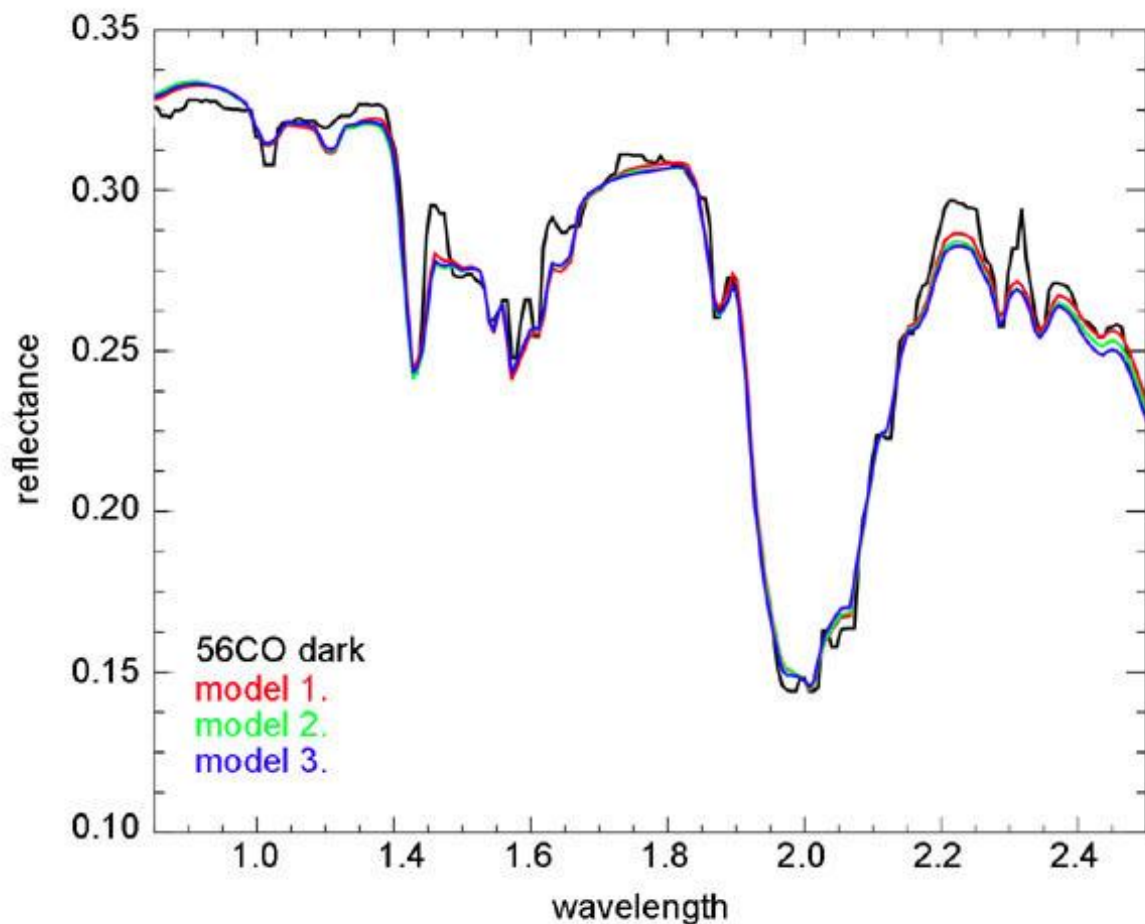
1072 Fig. 13. Fraction of water ice spectra with 1 micron grain size from the total water ice content  
1073 (grain size with 1 micron and 100 microns) as a function of time for the four units (see legend  
1074 of Fig. 5). Dark core show the smaller grain size fraction. Grey ring and bright halo have  
1075 intermediated grain size. Undisturbed terrains have the highest grain size. There is a general  
1076 trend with increasing grain size from  $L_S=180$  to 220 and then decreasing from  $L_S=220$  to 240.



1077

1078

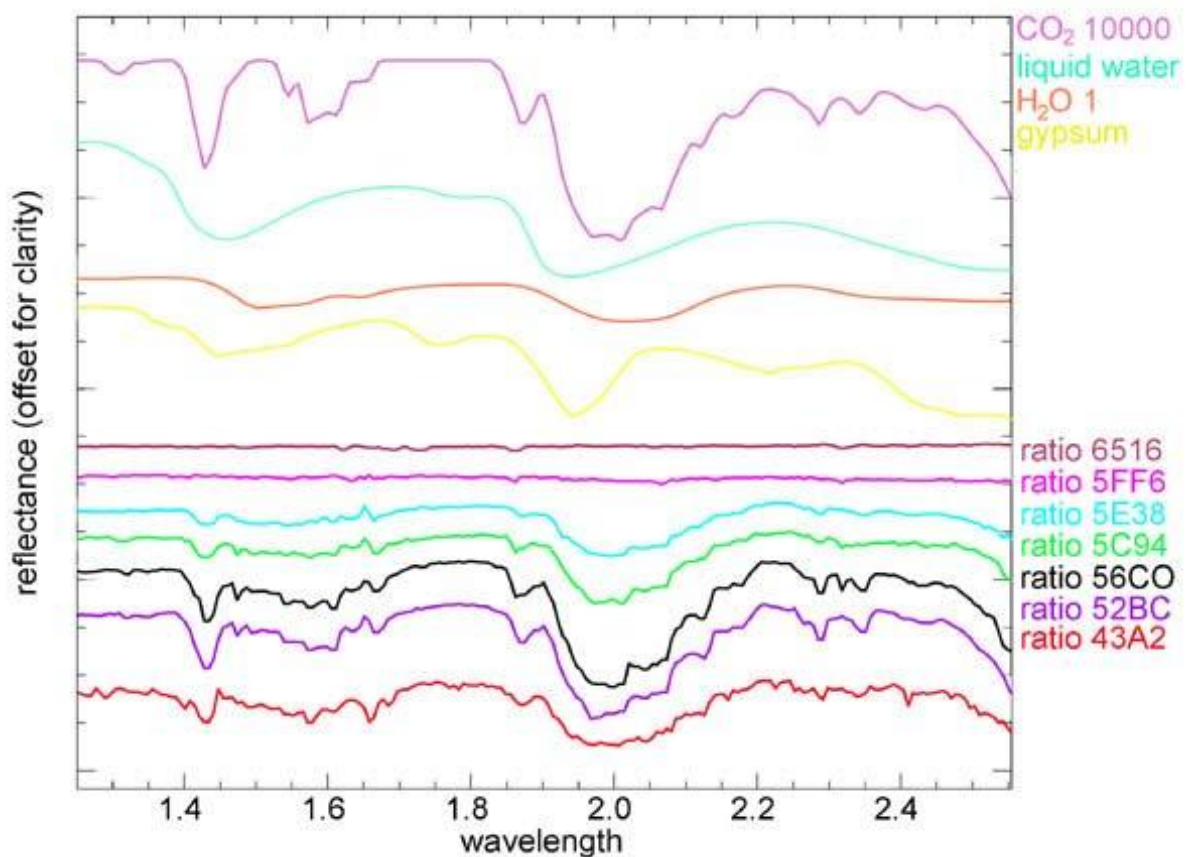
1079 Fig. 14. Best synthetic spectra obtained by sparse linear mixture of reference database using  
1080 FCLS algorithm versus observed spectra for the observation image no. 56CO dark core.  
1081 Model 3 database include all spectra described in Fig. 12. In this case, liquid water is detected  
1082 with an abundance of 0.04% and gypsum with an abundance of 1.57 % (rms=0.0056). Model  
1083 2 represents the same inversion with liquid water (1.46%) but without gypsum (rms=0.0058).  
1084 Model 1 represents the same inversion without gypsum, nor liquid water (rms=0.0059).  
1085 CRISM signal to noise ratio is 300 and thus errors bars cannot be seen in this figure. The rms  
1086 is slightly decreasing from model 1 to model 3, indicating the possible presence of liquid  
1087 water or gypsum but non-linear radiative transfer inversion has to confirm this trend.



1088

1089

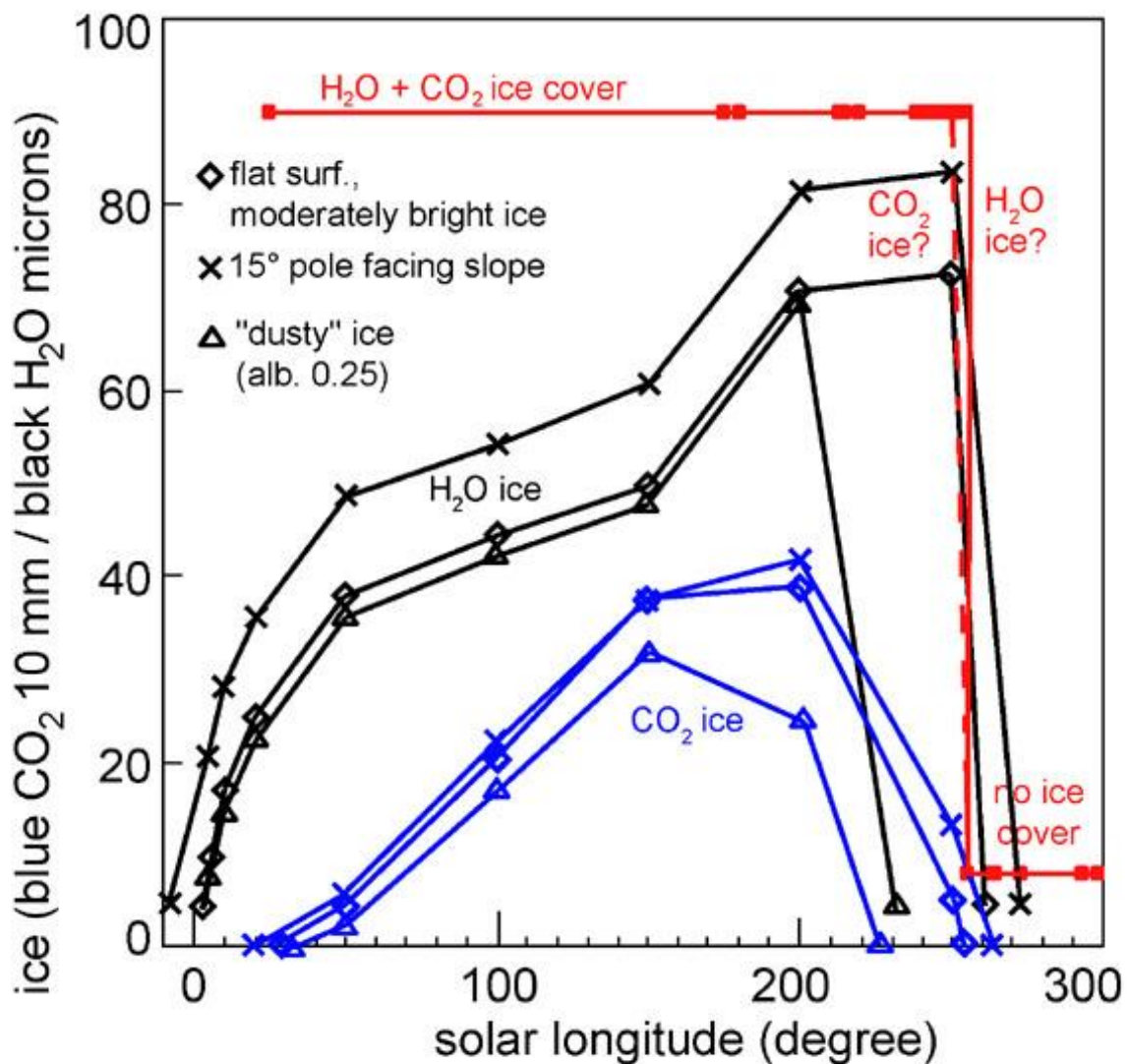
1090 Fig. 15. The 4 first spectra at the top correspond to reference spectra (see Fig. 11) for CO<sub>2</sub> ice,  
 1091 water ice, liquid water and gypsum. Below ratio between undisturbed ice terrain divided by  
 1092 dark core for seven CRISM observations are visible: 43A2 (L<sub>S</sub>=181.7°), 52BC (L<sub>S</sub>=213.7°),  
 1093 56CO (L<sub>S</sub>=221.0°), 5C94 (L<sub>S</sub>=241.7°), 5E38 (L<sub>S</sub>=245.5°), 5FF6 (L<sub>S</sub>=248.7°) and 6516  
 1094 (L<sub>S</sub>=262.6°). None of the ratio is compatible neither with gypsum nor with liquid water but  
 1095 with decreasing water ice and CO<sub>2</sub> ice compounds, strongly indicating that both water ice and  
 1096 CO<sub>2</sub> ice are present at the ground. The abundances of liquid water and gypsum, estimated by  
 1097 FCLS (model 3) on these ratio spectra, are always 0%. These results suggest that neither  
 1098 liquid water nor gypsum are enriched in the scene and therefore are presumably absent or in  
 1099 very small quantities.



1100

1101

1102 Fig. 16. Result of the model run on annual frost formation for H<sub>2</sub>O ice (black) and CO<sub>2</sub> ice  
 1103 (blue), plus the observed presence of any kind of ice at the target location from CRISM data  
 1104 (red). It shows as a function of L<sub>S</sub> (degree, horizontal axis) the cumulative thickness of CO<sub>2</sub>  
 1105 and H<sub>2</sub>O ice condensed on the ground, on the vertical axis the thickness of H<sub>2</sub>O and CO<sub>2</sub> are  
 1106 present using different scales, for CO<sub>2</sub> up to 40 cm and H<sub>2</sub>O up to 80 μm thickness.  
 1107 Diamonds, triangles and crosses correspond to 3 hypotheses for model parameters related to  
 1108 ground properties (see text for details).



1109

1110